


Cite this: *RSC Adv.*, 2025, 15, 38105

Mn²⁺ and [Ru(bpy)₃]²⁺ in UiO-67 metal organic frameworks enhance photocatalytic oxidation of benzylamine *via* an electron transfer pathway

Subrata Mandal,^a Novitasari Sinambela,^a Johannes Biskupek,^b Riccarda Müller,^c Ute Kaiser,^b Kerstin Leopold,^c and Andrea Pannwitz^{*def}

The selective oxidation of amines to imines is an essential transformation in many chemical syntheses. Driving such reactions with light and earth abundant catalysts is highly interesting in the context of solar light energy conversion and broadening the reaction scope in organic synthesis. The here reported bimetallic metal–organic framework (MOF), UiO-67 Ru₅₀-Mn₁₀, allows oxidation of benzylamine under ambient conditions *via* dual electron and energy transfer with oxygen. UiO-67 Ru₅₀-Mn₁₀ integrates [Mn(bpy)₂(Cl)₂] active sites and light-active [Ru(bpy)₃]²⁺ photosensitizers at the linkers of the UiO-67 scaffold. The spatial organisation of photo and redox-active centres enables efficient charge separation and mass transport. Under 460 nm LED irradiation for 24 h and ambient aerobic conditions, UiO-67 Ru₅₀-Mn₁₀ catalyses the oxidation of benzylamine to *N*-benzylidene-1-phenylmethanamine with turnover numbers up to 634, which is 1.6 to 1.8 times higher than homogeneous analogues and the Mn-free UiO-67 Ru₅₀. Structural and spectroscopic studies confirm successful incorporation of both metals, while mechanistic analyses reveal dual electron and energy transfer pathways, influenced by the solvent environment. This work highlights the potential of heterometallic MOFs with earth-abundant catalytic sites as efficient platforms for photocatalytic oxidative transformations.

Received 24th June 2025
Accepted 1st October 2025

DOI: 10.1039/d5ra04503g

rsc.li/rsc-advances

Introduction

The selective oxidation of amines to imines is an essential transformation in organic synthesis, with applications in fine chemicals, pharmaceuticals, and industrial catalysis. Traditionally, these reactions require harsh oxidants and elevated temperatures, making the development of efficient, sustainable, and photocatalytic alternatives highly desirable.¹ Among various traditional photocatalytic systems, such as TiO₂ and CdS, which have poor structure adjustment and low photocatalytic efficiency,^{2,3} metal–organic frameworks (MOFs) have gained significant attention due to their tunable porosity, structural flexibility, and ability to integrate very specific molecular photosensitizers (PSSs) and catalytic centres (CATs)

within a single platform.⁴ Considering the success of MOFs in artificial photosynthesis,^{5,6} significant efforts have focused on using them as carriers for catalysts, photosensitizers (PSs), or both, to enhance charge transfer and unlock new catalytic pathways for improved efficiency and selectivity in photocatalytic oxidation reactions.⁷ Additionally, the heterogeneous nature of MOF-based systems offers superior recyclability and stability, which are often challenging to achieve with their homogeneous counterparts.⁵

For example, Li and co-workers reported the oxidation reactions of a series of amines to imines with conversion yields of around 41–99% and selectivity of around 45–90% using molecular O₂ as an oxidant over the MOF NH₂-MIL-125(Ti) under visible light irradiation.⁸ Bai *et al.* reported that the MOF LTG-NiRu, constructed from a [Ru(phen)₃]²⁺-derived linker and Ni²⁺-functionalized nodes, exhibited exceptional catalytic activity in the aerobic photocatalytic oxidative coupling of amine derivatives, achieving nearly 100% conversion of benzylamines within 1 h under visible light.⁹ Jin and co-workers developed a mixed-linker Zr-MOF incorporating both electron donor and acceptor linkers based on naphthalene diimide and porphyrin, which showed high photocatalytic activity for aerobic oxidative coupling of benzylamine.¹⁰ However, in such systems, catalytic activity or charge separation often occurs between the parent linker and the secondary building unit (SBU), which can result in partial framework degradation.¹¹

^aInstitute of Inorganic Chemistry I, University Ulm, Albert-Einstein-Allee 11, 89081 Ulm, Germany

^bCentral Facility of Electron Microscopy, Electron Microscopy Group of Material Science, University of Ulm, Albert-Einstein-Allee 11, Ulm 89081, Germany

^cInstitute of Analytical and Bioanalytical Chemistry, University Ulm, 89081 Ulm, Germany

^dInstitute for Inorganic and Analytical Chemistry, Friedrich-Schiller-University Jena, Humboldtstr. 8, 07743 Jena, Germany. E-mail: Andrea.pannwitz@uni-jena.de

^eCenter for Energy and Environmental Chemistry Jena (CEEC), Friedrich-Schiller-Universität Jena, Philosophenweg 7a, 07743 Jena, Germany

^fHelmholtz Institute for Polymers in Energy Applications Jena (HIPOLE Jena), Lessingstraße 12-14, 07743 Jena, Germany


Although the latter one is stable, it lacks defined active sites and selective reaction pathways.

Incorporation of PS and single-site catalysts into a MOF represents a very interesting field for other photocatalytic reactions, such as the H₂ evolution reaction (HER),^{12,13} CO₂ reduction reaction (CO₂RR),^{14–17} and alcohol oxidation,¹⁸ however, their application related to benzylamine oxidation is rarely explored.

Nature's Photosystem II (PS II) provides a blueprint for light-driven, redox chemistry through the precise arrangement of a chlorophyll-based photosensitizer (P680) and a Mn₄CaO₅ cluster that catalyses water oxidation.¹⁹ While synthetic molecular models of PSII have largely aimed to replicate water oxidation,²⁰ often using Ru-based photosensitizers linked to manganese centres,^{21,22} the potential of such systems for alternative oxidative transformations remains underexplored.

In this study, a Ru(bpy)₃²⁺-functionalized MOF (UiO-67 Ru_x) was synthesized and further modified by coordinating Mn²⁺ sites *via* post-synthetic modification (PSM) to the bipyridine linkers of the framework, yielding the bimetallic system UiO-67 Ru_x-Mn_y. The concept is based on leveraging the structural stability and modularity of the UiO-67 backbone to organize photoactive ruthenium complexes and redox-active manganese centres in proximity, mimicking the compartmentalized environment of natural photosystem II. The resulting hybrid material was explored as a visible-light-responsive catalyst for the oxidative conversion of benzylamine to imine in aerobic conditions, and its activity was benchmarked against related systems, mono-functionalized analogues (UiO-67 Ru and UiO-67 Mn), and homogeneous reference complexes such as Ru(bpy)₃²⁺ and Mn(bpy)₂Cl₂. To validate successful Ru and Mn integration and preserve framework structure, multiple analytical tools were employed, including X-ray diffraction (XRD), infrared (IR) spectroscopy, nuclear magnetic resonance (NMR) spectroscopy, transmission electron microscopy (TEM), and X-ray photoelectron spectroscopy (XPS). To probe charge separation and electron-transfer behaviour, a combination of steady-state and time-resolved spectroscopic techniques, UV-vis absorption, photoluminescence quenching, and time-resolved emission, was employed, along with electrochemical studies.

This work sheds light on the cooperative effects between integrated light-absorbing and catalytic centres in MOF-based systems, offering new directions for the rational design of high-performance photocatalytic platforms for oxidative reactions.

Results and discussion

Synthesis and characterization

The UiO-67 MOFs of 2,2'-bipyridine-5,5'-dicarboxylate (bpydc)-based linker functionalized with Ru-based PS and single-site Mn catalyst were achieved *via* a two-step self-assembly process to yield composite photocatalytic systems (UiO-67 Ru_x-Mn_y) with an elemental ratio of Ru/Mn (*x*:*y* = 5:1 and 1:1). In these processes, the MOFs UiO-67 Ru_x-Mn_y (10:10 and 50:10) were designed and synthesized by a mixed-ligand synthetic strategy to introduce the Ru-units, and subsequently post-synthetic

metalation (PSM) to introduce the Mn-sites. The metallo-ligand linker [Ru(H₂bpydc)(bpy)₂]Cl₂ was prepared according to the previously published method.²³ The red coloured MOFs UiO-67 Ru₁₀ and UiO-67 Ru₅₀ (10 and 50% Ru respective to the bpydc) were synthesized by carefully adjusting the ratio of 2,2'-bipyridine-5,5'-dicarboxylic acid (H₂bpydc) and [Ru(H₂bpydc)(bpy)₂]Cl₂ to react with ZrCl₄ under solvothermal conditions and in presence of benzoic acid (BA) in *N,N*-dimethylformamide (DMF) at 120 °C (Fig. 1).²⁴ To generate control samples, white colour UiO-67 was synthesized by using only the H₂bpydc. The PSM of UiO-67 Ru_x and UiO-67 were performed by treating those nanocrystals with feed amounts of 10% (relative to the bpydc) MnCl₂ and 10% additional bipyridine (bpy) solution in ethanol (Fig. 1).

The crystallinity of these UiO-67 MOFs was maintained well in UiO-67-Ru_x and UiO-67 Ru_x-Mn₁₀ and UiO-67 Mn₁₀, which was confirmed by PXRD patterns similar to that of the here synthesized reference UiO-67 (Fig. 2a). Moreover, each phase exhibited characteristic reflection planes (111), (200), (220), (311), (222), and (400) at angles 5.7°, 6.6°, 9.3°, 10.9°, 11.4°, and 13.2°, respectively, confirming that they are isostructural to the reported face-centred cubic phase of UiO-67 (bpdcc) (bpdcc = biphenyl dicarboxylate) with the space group *Fm3m*.²⁵ This unique topology of UiO-67 (Fig. S5) has a periodic structure with an ideal unit cell formula of Zr₆O₄(OH)₄(BPDC)₆, where this cluster adopts an octahedral geometry with six Zr(IV) cations occupying its vertices.²⁶ Successful incorporation of Ru and Mn moieties was supported by diffuse reflectance UV/vis spectroscopy. A broad absorption (~400–700 nm) in the spectrum of UiO-67 Ru₅₀-Mn₁₀ was consistent with the absorption of UiO-67 Ru₅₀, which can be attributed to the metal-to-ligand charge transfer (MLCT) absorption of [Ru(bpy)₃]²⁺ moiety in the UiO-67 framework (Fig. 2b). An increase in the absorption edge and blue shift of the highest absorption MLCT band compared to spectra of homogenous [Ru(H₂bpydc)(bpy)₂]²⁺ (Fig. S2) can be attributed to the immobilization effect of the complex in a rigid environment.²⁷ The immobilization of the Mn complex, however, is not distinguishable, but can be supported by studying the diffuse reflectance UV-visible spectroscopy of the control UiO-67 Mn₁₀ counterparts. As shown in Fig. 2b, an additional broad absorption in the range of 360–500 nm in UiO-67 Mn₁₀ is observed compared to that of pristine UiO-67, resulting in a yellow colored solid (Fig. 2b, inset), which can be attributed to the absorption resulting from the Mn-complex.²⁸ Compared to the spectra of its homogeneous molecular model [Mn(bpy)₂Cl₂] (Fig. S2), a significant red shift in the MOF can be ascribed to the role of the solvent effect on the absorption band, tentatively assigned to an MLCT.²⁸

The TEM images of UiO-67 Ru₅₀ and UiO-67 Ru₅₀-Mn₁₀ (Fig. 1c) reveal that both samples exhibit a well-defined octahedral crystalline morphology, with crystal sizes ranging from approximately 1 to 2 μm. Notably, no significant morphological changes are observed when compared to their UiO-67 and UiO-67 Mn₁₀ counterparts. However, a pronounced difference in crystal size is evident: UiO-67 and UiO-67 Mn₁₀ crystals are considerably smaller, typically ranging from 200 to 500 nm. This variation in crystal size is likely attributed to differences in



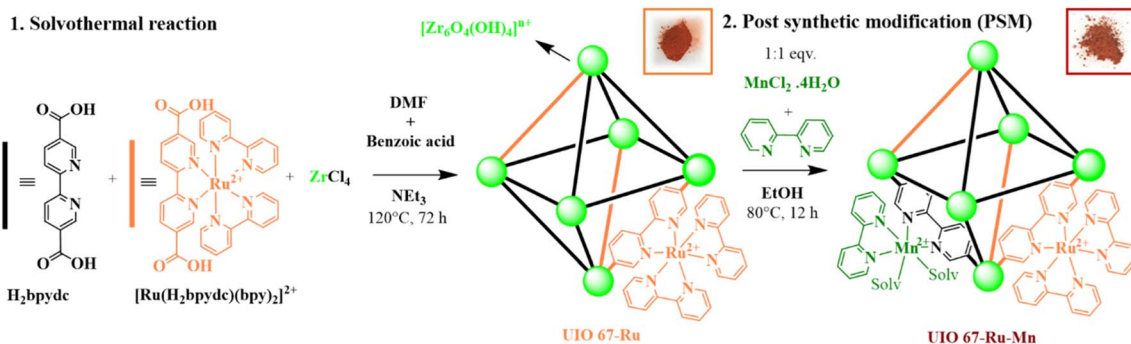


Fig. 1 Synthetic procedure of UiO-67 Ru-Mn via solvothermal synthesis and PSM.

reaction kinetics between Zr(IV) and the H₂bpydc linker vs. the [Ru(H₂bpydc)(bpy)₂]₂ complex. Additionally, factors such as linker acidity, solubility, and geometry, which are altered upon metalation, can significantly affect the nucleation and growth processes during synthesis, ultimately influencing the final crystal size.²⁹ Notably, in both cases, post-synthetic modification (PSM) for Mn incorporation does not result in any observable changes in crystal size or shape, indicating that the overall framework integrity remains unaffected.

High-angle annular dark-field scanning transmission electron microscopy (HAADF-STEM) images together with corresponding energy dispersive X-ray (EDX) element mappings of

UiO-67 Ru₅₀-Mn₁₀ are shown in Fig. 3 and S6, S7, SI, for UiO-67 Ru₅₀, respectively. The HAADF-STEM and EDX images clearly show the presence of elements Zr, C, N, O, Cl, and Ru, which are distributed throughout the entire structure of each MOF. The signals for Mn were detected in UiO-67 Ru₅₀-Mn₁₀. Unlike C, N, O, and Zr in both the framework, the Ru, Cl in both the framework, and Mn metals in UiO-67 Ru₅₀-Mn₁₀ appear to be more spatially isolated. This observation may be attributed either to the separation of individual metal-complex centers within the linker motif, as enforced by the framework structure, or to the relatively low composition of these elements in the overall material. Notably, the EDX spectra of these MOFs

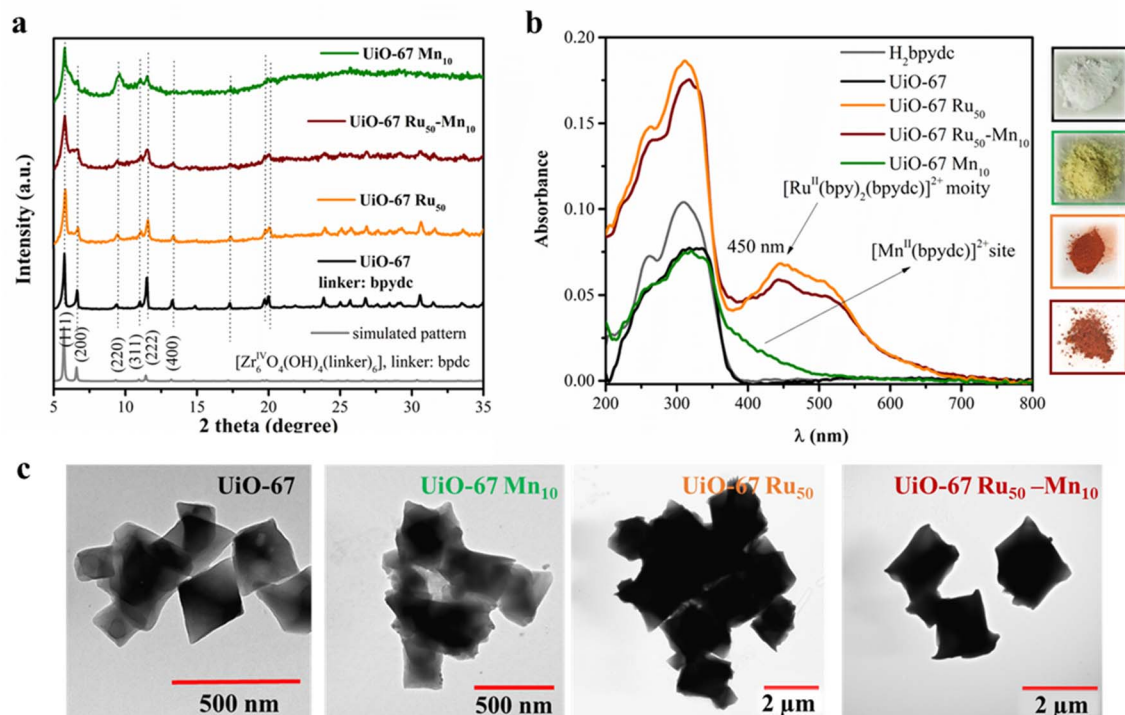


Fig. 2 (a) PXRD patterns of UiO-67 Ru₅₀-Mn₁₀ and their counterparts (UiO-67, UiO-67 Mn₁₀, UiO-67 Ru₅₀) and the simulated XRD pattern of UiO-67 made up of biphenyl dicarboxylate (bpdc) linker obtained from the crystallographic data reported earlier,²⁵ and their (b) UV-vis absorption spectra obtained from the solid-state diffuse reflectance spectroscopy. Inset on the right side of the figures shows the photograph of the prepared samples. (c) Transmission electron microscopic (TEM) images of the UiO-67, UiO-67 Mn₁₀, UiO-67 Ru₅₀, and UiO-67 Ru₅₀-Mn₁₀ (from left to right). The colour code of the MOFs is as follows: black = UiO-67, green = UiO-67 Mn₁₀, orange = UiO-67 Ru₅₀, and brown = UiO-67 Ru₅₀-Mn₁₀.

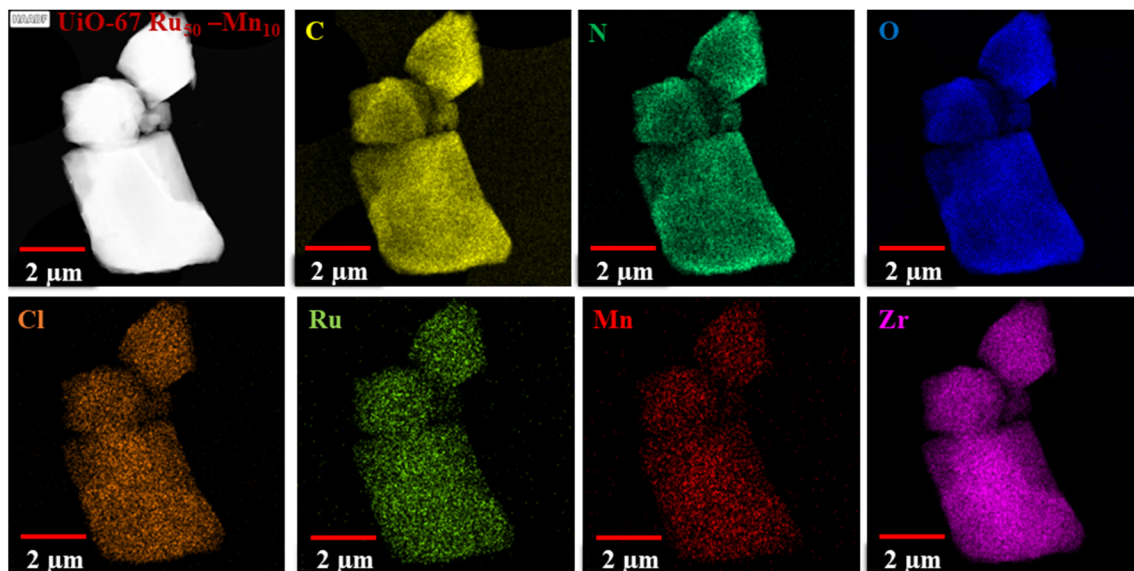


Fig. 3 High-angle annular dark field scanning transmission electron microscopic (HAADF-STEM) image with corresponding EDX element mapping images of UiO-67 Ru₅₀-Mn₁₀. The yellow, dark green, blue, orange, light green, red, and purple signals represent C, N, O, Cl, Ru, Mn, and Zr, respectively. Please note, that the Mn-mapping is mostly an artifact due to overlapping of Mn-K β lines with Fe-K α lines that originate from stray electrons on the TEM column made of iron.

(Fig. S6, S7 and Table S2, SI) confirm the presence of Ru and Cl signals; however, the Mn signal observed in UiO-67 Ru₅₀-Mn₁₀ arises from the overlap of the Mn K β line with the Fe K α line, where Fe originates from stray electrons scattered on the TEM column made of iron. Consequently, the Mn elemental map should largely be regarded as an artifact. The experimentally determined average Zr/Ru ratios for UiO-67 Ru₅₀ and UiO-67 Ru₅₀-Mn₁₀ are ~ 1.12 – 6.35 and ~ 11.4 , respectively. These values deviate significantly from the expected stoichiometric ratio of Zr/Ru = 2, according to the ideal formulas: UiO-67 Ru₅₀ ($[\text{Zr}_6\text{O}_4(\text{OH})_4(\text{bpydc})_3] \cdot 3[\text{Ru}(\text{bpy})_2(\text{bpydc})]\text{Cl}_2$) and UiO-67 Ru₅₀-Mn₁₀ ($[\text{Zr}_6\text{O}_4(\text{OH})_4(\text{bpydc})_{2.4}] \cdot 3[\text{Ru}(\text{bpy})_2(\text{bpydc})]\text{Cl}_2 \cdot 0.60[\text{Mn}(\text{bpy})(\text{bpydc})\text{Cl}_2]$). This discrepancy suggests that the distribution of Ru within the framework is random and that both MOFs deviate from their idealized formulas, either due to residual solvent molecules from the synthesis or the presence of linker vacancies.

The chemical compositions of UiO-67 and UiO-67-Ru_x were determined by ^1H -NMR measurements in DMSO- d_6 by digesting them in DCl/D₂O (see SI page 8–9 for detailed calculations). A previous report had suggested that benzoic acid is commonly entrapped within the pore of the MOF and, consequently, cannot be completely removed during the washing process.³⁰ In our case, the ^1H -NMR spectrum displayed similar signals corresponding to benzoate, while the presence of a negligible amount of formate (HCOO^-) is there, although formate was not used in the initial synthesis, this molecule was produced due to the decomposition of DMF during the solvothermal reaction (Fig. S8).³⁰ These molecules likely participate in the Zr-cluster assemblies similar to some Zr-MOFs, where the modulators were identified in the crystal structures.^{30,31} As the formate peak is negligible it is ignored for the

current analysis. Based on the integration of the signals of BA, including the bpydc, the chemical formula of UiO-67 was estimated to be $[\text{Zr}_6\text{O}_4(\text{OH})_4(\text{bpydc})_{5.82}(\text{BA})_{0.36}]$ (Table S3). In UiO-67 Ru₅₀ and UiO-67 Ru₁₀, the $[\text{Ru}(\text{bpy})_2(\text{bpydc})]\text{Cl}_2$ moiety can be characterized by ^1H NMR, and analysis was possible because it remains intact under these MOF digestion conditions (Fig. S8). Based on the integration of the proton resonances for $[\text{Ru}(\text{bpy})_2(\text{bpydc})]\text{Cl}_2$ in UiO-67 Ru₅₀, and UiO-67 Ru₁₀ the chemical formula was estimated to be $[\text{Zr}_6\text{O}_4(\text{OH})_4(\text{bpydc})_{4.724}(\text{BA})_{1.13}] \cdot 0.7[\text{Ru}(\text{bpy})_2(\text{bpydc})]\text{Cl}_2$, and $[\text{Zr}_6\text{O}_4(\text{OH})_4(\text{bpydc})_{5.48}(\text{BA})_{0.71}] \cdot 0.16[\text{Ru}(\text{bpy})_2(\text{bpydc})]\text{Cl}_2$, respectively, and the degree of Ru modification in UiO-67 Ru_x MOFs is 13% and 3%, respectively, indicating that complete incorporation of the Ru moiety did not take place. Unfortunately, the quantification of Mn quantification *via* NMR is not possible, as Mn^{2+} is paramagnetic, resulting in a broad signal as observed in UiO-67 Ru₁₀-Mn₁₀ (Fig. S8).

X-ray photoelectron spectroscopy (XPS) was used to determine the precise elemental composition, the integrity of the Ru and Mn complexes, and their electronic states within the MOFs (Fig. 4a). All shifts for the samples were corrected by normalizing the C (1s) binding energy to 284.8 eV (Fig. S9a). In all the MOFs, including C 1s, all characteristic peaks for Zr 3d at 180.95–187.05 eV (Fig. 4b), N 1s at 395.90–402.30 eV (Fig. S9b), and O 1s at 528.00–535.50 eV^{32,33} (Fig. S9c) were observed, corresponding to the primary backbone (linker and SBU), and notably, slight changes are observed in UiO-67-Ru₅₀, and UiO-67 Ru₅₀-Mn₁₀ MOFs for the local environment exerted by the Ru and Mn molecular moieties. For instance, the binding energy of N 1s in UiO-67 is 398.2 eV, which is attributed to N in bpydc²⁻ (Fig. S9b). The electron density of nitrogen at this region was reduced, followed by the formation of coordination interactions



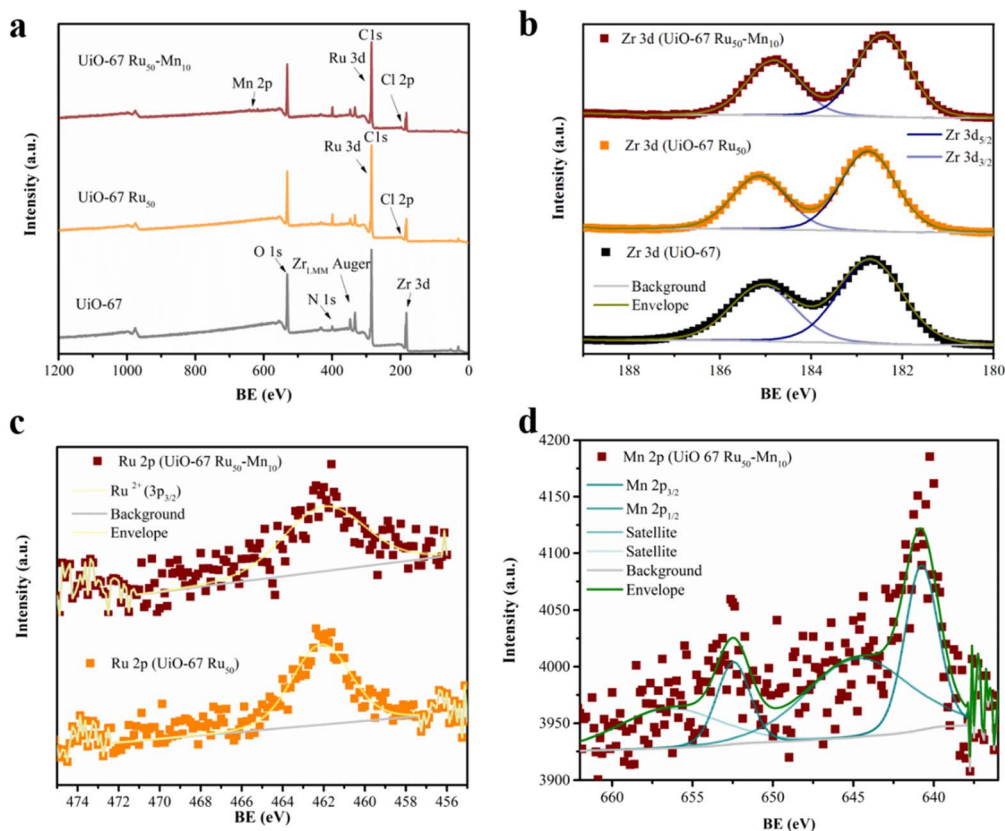


Fig. 4 X-ray photoelectron spectra (XPS) of UiO-67-based materials: (a) survey spectra of UiO-67, UiO-67 Ru₅₀, and UiO-67 Ru₅₀-Mn₁₀; (b) high-resolution Zr 3d spectra for all three samples; and (c) high-resolution Ru 2p spectra for UiO-67 Ru₅₀ and UiO-67 Ru₅₀-Mn₁₀ and (d) Mn 2p for UiO-67 Ru₅₀-Mn₁₀. BE = binding energy.

between bpydc²⁻ and the Ru²⁺ and Mn²⁺ species in UiO-67 Ru₅₀ and UiO-67 Ru₅₀-Mn₁₀, leading to distinct N 1s peaks at 398.6 eV and 399.00 eV, respectively. The change in the peak of N 1s to higher binding energy indicates that the N atom on the bipyridine (bpydc²⁻) is coordinated with the Ru ion in UiO-67 Ru₅₀ and Ru and Mn ions, which reduces the electron density at the N atom.^{34,35} Additionally, in contrast to UiO-67, for both UiO-67 Ru₅₀ and UiO-67 Ru₅₀-Mn₁₀, two peaks are apparent in the Ru regions at 285.37 and 281.12 eV, which are assigned to Ru²⁺ 3d_{3/2} and 3d_{5/2}, respectively (Fig. S9a) which almost overlaps with the C 1s signal (Fig. 4a). Fig. 4c shows the respective peaks at around 462.12 eV assigned to the Ru 2p_{3/2} region and, which are in good agreement with the pattern of divalent ruthenium, Ru²⁺.¹² No other valence state peaks, such as Ru³⁺ or Ru⁴⁺, were detected. The Mn 2p spectra (Fig. 4d) observed in UiO-67 Ru₅₀-Mn₁₀ contain two main peaks centred at 640.75 eV (Mn 2p_{3/2}) and 652.5 eV (Mn 2p_{1/2}), while no Mn³⁺ and Mn⁴⁺ species are observed, which are generally observed at higher energies than the Mn²⁺ species. Additionally, the spectra consist of satellite peaks with considerable intensity at ~5 eV higher binding energy (645.10 eV) compared to that of the corresponding main Mn 2p_{3/2} peak. These spectral features reflect that the valence of the central manganese ion in the UiO-67 Ru₅₀-Mn₁₀ is +2 (ref. 36 and 37) and [Mn(bpy)(bpydc)Cl₂] remained stable during the PSM process. It should be noted that the Cl 2p peaks in UiO-67 Ru₅₀ and UiO-67 Ru₅₀-Mn₁₀

MOFs at around 195.25–201.62 eV exist (Fig. S9d), representing Cl anion as a counter anion.

Despite the presence of the Ru peak being detected in UiO-67 Ru₅₀-Mn₁₀, Ru was not taken into account for estimating the Ru/Mn ratio due to the overlap with C and a weak signal. Therefore, the Zr/Mn ratio was considered instead, which was found to be 7.73 in UiO-67-Ru₅₀-Mn₁₀. Combined with the Zr : Ru ratio of 8.57 obtained from NMR analysis of UiO-67-Ru₅₀ (assuming no leaching occurred during the post-synthetic modification, PSM), these measurements allowed the estimated atomic ratio of Zr : Ru : Mn to be calculated as 1 : 0.117 : 0.129. Based on this, the proposed chemical formula of UiO-67 Ru₅₀-Mn₁₀ is: [Zr₆-O₄(OH)₄(bpydc)_{3.944}(BA)_{1.13}·0.70[Ru(bpy)₂(bpydc)]Cl₂·0.78 [Mn(bpy)(bpydc)Cl₂]. In accordance with the above formulation, the molar Ru/Mn ratio is nearly 0.89. This ratio is expected to be reflected in the high resolution-continuum graphite furnace atomic absorption spectrometry (HR-CS-GFAAS) and total X-ray fluorescence spectrometry (TXRF) measurements of the MOF (see SI for details and Fig. S10). Indeed, the element analysis in Table S5 confirms that the Ru/Mn molar ratio is ~1.02, providing excellent corroboration of the structural formulation.

Photocatalytic activity for the oxidation of benzylamine

The photocatalytic oxidation of benzylamine was carried out under ambient conditions using the synthesized MOFs as



catalysts. Reactions were performed in a mixed solvent system of acetonitrile:H₂O (4:1 v/v) under an air atmosphere. The reaction setup utilized a 3D-printed modular photoreactor equipped with a 460 nm LED light source (800–1250 mW) operating at a current of 0.7 A and a voltage of 4 V.^{27,30} The reaction progress was initially monitored under radiation for 36 h (Fig. S11), and the imine product *N*-benzylidene-1-phenylmethanamine formed after 24 h for each set of reactions were quantified using ¹H NMR spectroscopy, with 1,3,5-trioxane employed as an internal standard (see SI page 17 for details and Fig. S12), and the yields (%) calculated for the conversion to *N*-benzylidene-1-phenylmethanamine are listed in Table 2.

The control experiments under dark conditions, in absence of any catalyst or MOF are listed in Table 2 entries 5 and 6 and yielded no detectable oxidation products, confirming the necessity of both light and the MOF catalyst for photocatalytic activity. Among the tested materials, UiO-67-Ru₅₀ and UiO-67 Ru₅₀-Mn₁₀ exhibited significant catalytic activity for the oxidation of benzylamine to the corresponding imine (*N*-benzylidene-1-phenylmethanamine) with yields of 27.6% (selectivity 75%) and 45.1% (selectivity 85%), respectively. Notably, no significant imine products under the light-irradiation were observed for the other two counterparts, UiO-67 (yield = 1%) and UiO-67 Mn₁₀ (yield = 0.2%), indicating that both light and the Ru moiety are essential components for catalytic activity. In particular and according to the kinetic study, UiO-67 Ru₅₀-Mn₁₀ showed superior fast performance with a rate of 6895 μmol g_{MOF}⁻¹ h⁻¹. This rate is enhanced compared to UiO-67 Ru₅₀ (4218 μmol g_{MOF}⁻¹ h⁻¹) (Fig. 5a). The enhancement observed upon Mn²⁺ incorporation can be attributed to an improved charge transfer efficiency and the presence of additional catalytic sites facilitated by Mn²⁺ within the framework.

The influence of the solvent environment was tested *via* additional experiments in pure acetonitrile (CH₃CN). While the overall yield of imine products in photocatalysis with the MOFs was lower in pure CH₃CN, the observed trend in photocatalytic performance among the different MOFs matches the trend in the solvent mixture CH₃CN:H₂O (4:1 v/v). Specifically, UiO-67 Ru₅₀-Mn₁₀ with a yield of 14.6% (selectivity 94%) and rate of 2229 μmol g_{MOF}⁻¹ h⁻¹ continued to outperform UiO-67 Ru (yield: 11.9%, with selectivity 93% and rate: 1822 μmol g_{MOF}⁻¹ h⁻¹), highlighting the robustness of its superior activity regardless of the solvent conditions (Fig. 5a). Interestingly, compared to the CH₃CN/H₂O mixture, the oxidation reaction of benzylamine in CH₃CN alone proceeded with higher selectivity,

irrespective of the MOF photocatalysts. In aqueous media, a photocatalytic system can form hydroxyl radicals, which can oxidise the substrate and product indiscriminately, thereby reducing the selectivity of the reaction.³⁸

Furthermore, the effect of the Ru loading was examined. At low Ru concentrations, only minimal product formation was observed, with UiO-67-Ru₁₀ yielding 4.7% and UiO-67 Ru₁₀-Mn₁₀ yielding 3.7%. No consistent trend was observed at this range (Table 2), further underscoring the pivotal role of the Ru moiety as the primary photosensitizing centre. These findings highlight the necessity of an optimized Ru loading to achieve effective photocatalysis, emphasizing that suboptimal concentrations result in diminished activity, likely due to insufficient active sites for efficient light absorption. Atmospheric conditions were also found to be critical for the reaction. No product formation was observed when the reaction was conducted under an argon atmosphere (Table 2 entry 11), confirming the requirement of molecular oxygen as the terminal oxidant in the photocatalytic cycle.

To assess the role of the MOF-assembly, the homogeneous system was tested, using the molecular analogues [Ru(bpy)₂(bpydc)]Cl₂ ([Ru]) and [Mn(bpy)₂Cl₂]·H₂O ([Mn]) in respective combinations in CH₃CN/H₂O (v/v 4:1) and pure CH₃CN. As shown in Fig. 5b and Table 2, both molecular systems exhibit similar activity trends, with [Ru] alone (TON = 206) < [Ru] + [Mn] (TON = 382). However, their corresponding MOF systems, UiO-67-Ru₅₀ and UiO-67-Ru₅₀-Mn₁₀, display approximately 1.6-fold higher TONs (358 and 634, respectively) under identical conditions, highlighting the enhanced performance imparted by the heterogeneous framework.

Interestingly, under pure CH₃CN conditions, the homogeneous systems exhibited a strong increase in TON (643 for [Ru] alone and 763 for [Ru] + [Mn]). A kinetic analysis also revealed that the reaction plateau is reached more quickly in CH₃CN than in the CH₃CN/H₂O mixture (Fig. S13). This trend is opposite to that observed for their MOF counterparts (Table 2 and Fig. 5b) and might be attributed to differences in reaction pathways influenced by the solvent and the 3D-assembly in the MOF *vs.* the diffusion-controlled process in homogeneous conditions.^{39,40}

It is interesting to note that, similar to the MOF experiments, the combination of [Ru] and [Mn] in homogeneous solution outperforms [Ru] alone under all tested conditions, suggesting a synergistic interaction between the Ru and Mn components that is preserved even outside of the MOF matrix. More details of the proposed reaction pathways, including electron transfer

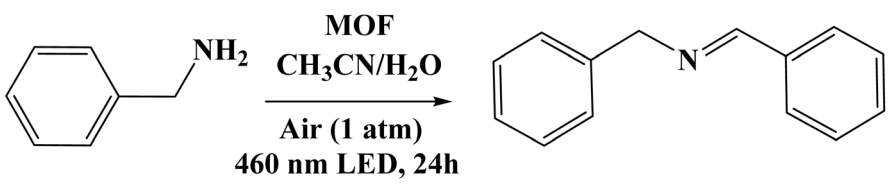
Table 1 Calculated formulas of the MOFs, according to ¹H NMR^a

Samples	Calculated formula of the MOF [Zr ₆ O ₄ (OH) ₄ (bpydc) _x (BA) _y]
UiO-67	[Zr ₆ O ₄ (OH) ₄ (bpydc) _{5.82} (BA) _{0.36}]
UiO-67 Ru ₅₀	[Zr ₆ O ₄ (OH) ₄ (bpydc) _{4.724} (BA) _{1.13}]·0.70[Ru(bpy) ₂ (bpydc)]Cl ₂
UiO-67 Ru ₁₀	[Zr ₆ O ₄ (OH) ₄ (bpydc) _{5.48} (BA) _{0.71}]·0.16[Ru(bpy) ₂ (bpydc)]Cl ₂
UiO-67 Ru ₅₀ -Mn ₁₀	[Zr ₆ O ₄ (OH) ₄ (bpydc) _{3.944} (BA) _{1.13}]·0.70[Ru(bpy) ₂ (bpydc)]Cl ₂ ·0.78[Mn(bpy) ₂ (bpydc)]Cl ₂

^a The ratio of Ru and Mn in UiO-67 Ru₅₀-Mn₁₀ MOF was calculated from the combination of ¹H NMR and XPS data in Tables S3 and S4.



Table 2 Photocatalytic benzylamine oxidative coupling reaction^a

							
#	Catalysts	Conditions	Yield ^b (%)	Selectivity ^b (%)	TON ^c	TOF ^c (h ⁻¹)	Rate (μmol g _{MOF} ⁻¹ h ⁻¹)
1	UiO-67	CH ₃ CN/H ₂ O 6 h	1.0	81	—	—	157
2	UiO-67 Mn ₁₀	CH ₃ CN/H ₂ O 6 h	0.2	76	—	—	28
3	UiO-67 Ru ₅₀	CH ₃ CN/H ₂ O 24 h	27.6	75	358	14.9	4218
4	UiO-67 Ru ₅₀ -Mn ₁₀	CH ₃ CN/H ₂ O 24 h	45.1	85	634	26.4	6895
5	UiO-67 Ru ₅₀ -Mn ₁₀	CH ₃ CN/H ₂ O 24 h, dark	—	—	—	—	—
6	No catalyst	CH ₃ CN/H ₂ O 6 h	—	—	—	—	—
7	UiO-67	CH ₃ CN, 24 h	1.4	77	—	—	213
8	UiO-67 Mn ₁₀	CH ₃ CN, 24 h	0.7	71	—	—	101
9	UiO-67 Ru ₅₀	CH ₃ CN, 24 h	11.9	93	154	6.4	1822
10	UiO-67 Ru ₅₀ -Mn ₁₀	CH ₃ CN, 24 h	14.6	94	205	8.5	2229
11	UiO-67 Ru ₅₀ -Mn ₁₀	CH ₃ CN/H ₂ O 24 h, Ar	—	—	—	—	—
12	UiO-67 Ru ₁₀	CH ₃ CN, 24 h	4.7	80	240	10.0	721
13	UiO-67 Ru ₁₀ -Mn ₁₀	CH ₃ CN, 24 h	3.7	79	193	8.1	564
14	[Ru]	CH ₃ CN/H ₂ O 24 h	15.7	88	206	8.6	—
15	[Ru] + [Mn]	CH ₃ CN/H ₂ O 24 h	29.1	93	382	15.9	—
16	[Ru]	CH ₃ CN, 24 h	49.5	94	648	27.8	—
17	[Ru] + [Mn]	CH ₃ CN, 24 h	58.2	99	763	31.0	—

^a Reaction condition: MOF (1 mg), CH₃CN : H₂O (4 mL, 4 : 1 v/v) or pure CH₃CN, benzylamine (80 μL, 0.734 mmol), (λ = 460 nm LED, 24 or 6 h), air (1 atm). ^b Determined by ¹H NMR using 1,3,5-trioxane as the internal standard. ^c For TON and TOF calculation Ru content was calculated from their respective MOF (1 mg) as per structure formula listed in Table 1. For homogeneous conditions: [Ru] = [Ru(bpy)₂(bpydc)]Cl₂, [Mn] = [Mn(bpy)₂Cl₂]·H₂O, 0.28 μmole of [Ru] was used.

between the Ru-photosensitizer and the Mn-unit, are discussed *vide infra*.

Reaction intermediates

Interestingly, a prominent reaction intermediate phenyl-methanimine (Im₁), along with a tentatively assigned

hemiaminal species *N*-benzyl-1-phenylmethanedi-amine (Im₂), were detected in the CH₃CN/H₂O (v/v 4 : 1) solvent mixture for both the homogeneous [Ru] system and the UiO-67 Ru₅₀ catalyst (Fig. 6a and b). In contrast, for UiO-67 Ru₅₀-Mn₁₀ and the homogenous [Ru] + [Mn] systems, although Im₁ was identified, the transient intermediate Im₂ was either absent (UiO-67 Ru₅₀-

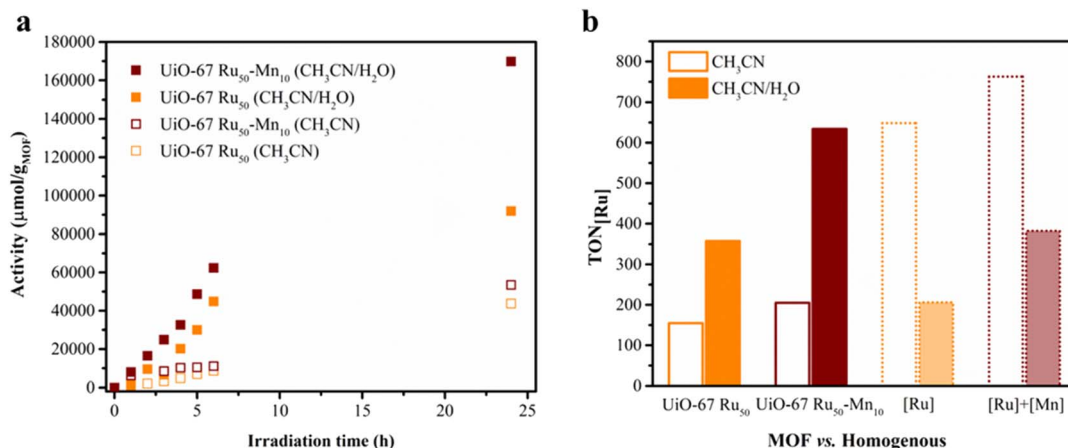


Fig. 5 (a) Photocatalytic activity (expressed as μmol g_{MOF}⁻¹ vs. time) for the oxidation of benzylamine in the presence of UiO-67 Ru₅₀ (orange) and UiO-67 Ru₅₀-Mn₁₀ (red) conducted in CH₃CN (hollow square) and CH₃CN/H₂O (v/v 4 : 1) (solid square). (b) A comparison of TON_[Ru] for the photocatalytic oxidation of benzylamine after 24 h of irradiation for the MOFs with homogeneous [Ru]: [Ru(bpy)₂(bpydc)]Cl₂ alone (transparent orange) and [Ru] + [Mn] ([Ru(bpy)₂(bpydc)]Cl₂ with [Mn(bpy)₂Cl₂]·H₂O) (transparent red), conducted in CH₃CN (hollow square) and CH₃CN/H₂O (v/v 4 : 1) (solid square).



Mn₁₀) or detected inconsistently ([Ru] + [Mn]), as indicated by the ¹H NMR spectra (Fig. 6b and S14–S17). This observation suggests that the hemiaminal species undergoes more rapid decay in the presence of Mn²⁺-incorporated catalysts, particularly UiO-67 Ru₅₀-Mn₁₀, than in UiO-67 Ru₅₀ or the homogeneous [Ru] system. The incorporation of Mn²⁺ likely accelerates the overall reaction rate by promoting a faster conversion of *N*-benzyl-1-phenylmethanediamine to the final imine product, *N*-benzylidene-1-phenylmethanamine. This may occur *via* enhanced electron or proton transfer steps, facilitating more efficient ammonia elimination.

In pure CH₃CN, no such intermediates were observed for either the MOF-based or homogeneous systems (Fig. 6c and S18–S21), suggesting that an alternative reaction mechanism predominates under non-aqueous conditions. Specifically, energy transfer from the ³MLCT (triplet metal-to-ligand charge transfer) state to oxygen, forming the reactive oxygen species ¹O₂ can yield to an alternative reaction pathway, followed by

rapid condensation of Im₁ and dehydration of Im₂, which is likely operative as discussed *vide infra*.

These findings highlight the critical absence or presence of water in modulating the reaction mechanism, modulating both the efficiency and the turnover frequency of the MOF-based catalysts. To further substantiate our observations, we compared the photocatalytic performance of UiO-67 Ru₅₀-Mn₁₀ with other MOF-based photocatalysts reported previously (Table 3). Since experimental parameters such as initial substrate concentration, catalyst loading, reaction time, and solvent systems vary significantly across studies, we adopted the rate of oxidative coupling (μmol g_{MOF}^{−1} h^{−1}) in CH₃CN as a basis for comparison. Compared to benzene dicarboxylate-based and amine functionalized MOFs: UiO-66, UiO-66 NH₂, and m-NH₂-MIL-125, n-NH₂-MIL-125 (Table 3 entries 1–3, and 6), our UiO-67 Ru₅₀-Mn₁₀ MOF exhibits a rate of 2229 μmol g_{MOF}^{−1} h^{−1}, which is nearly 16-, 8-, 5-, and 2-fold higher, respectively, under similar solvent conditions. Notably, the rate is quite relatable to the Ru(bpy)₃@MIL-125 system (Table 3 entry 5). Furthermore,

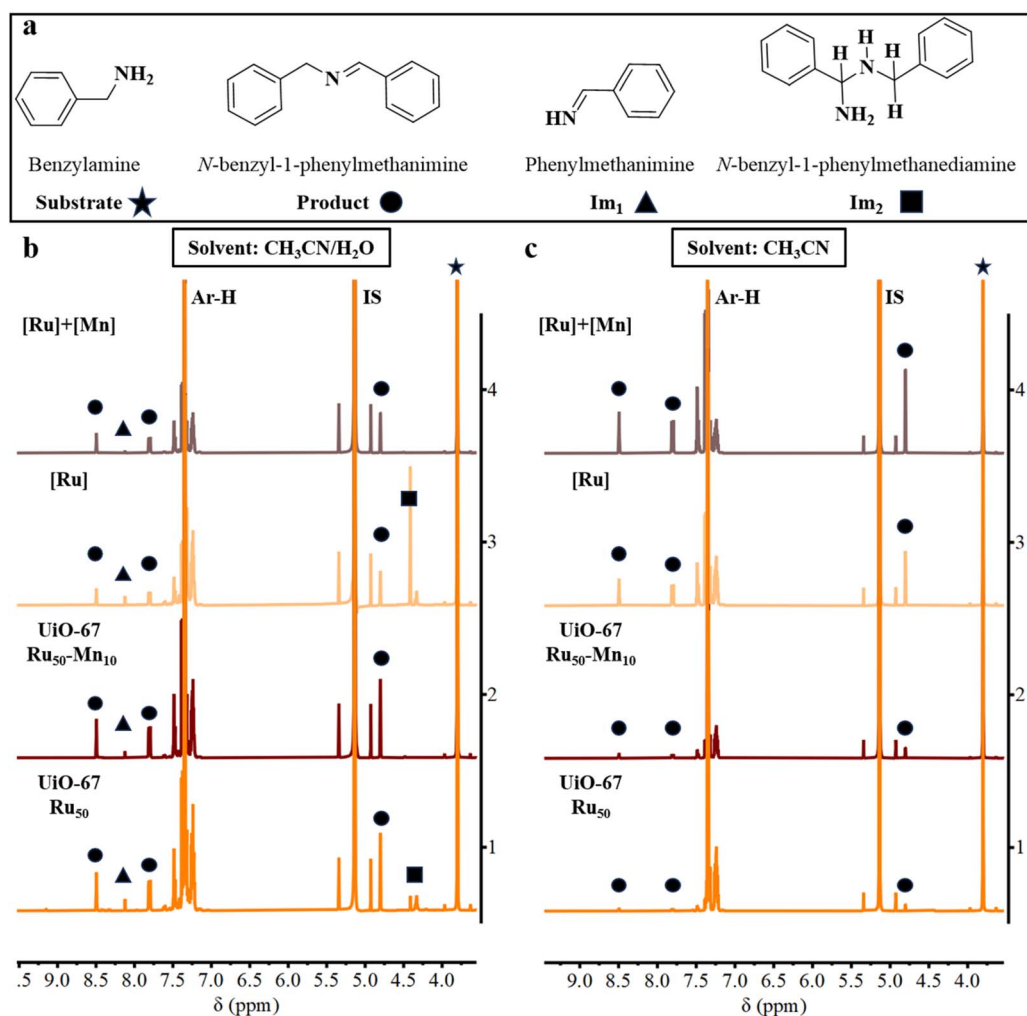


Fig. 6 (a) Molecules identified from the ¹H NMR spectra and (b and c) the corresponding spectra of reaction aliquots (in CD₃CN) collected at 4 h during the benzylamine oxidation in the presence of UiO-67 Ru₅₀, UiO-67 Ru₅₀-Mn₁₀ MOFs, homogeneous [Ru] ([Ru(bpy)₂(bpydc)]Cl₂), and the combination [Ru] + [Mn] ([Ru(bpy)₂(bpydc)]Cl₂ with [Mn(bpy)₂Cl₂]·H₂O) under (b) CH₃CN/H₂O (v/v 4 : 1) and (c) CH₃CN solvent conditions. IS = internal standard.



Table 3 Reported MOF-based photocatalysts for the oxidative coupling of benzylamine to *N*-benzylidene-1-phenylmethanamine

#	Catalysts	Solvent	Catalyst/ benzylamine	Light source, time	Conv. (%)	Selectivity (%)	Yield (%)	Rate ($\mu\text{mol g}_{\text{MOF}}^{-1} \text{h}^{-1}$)
1	UiO-66 (ref. 41)	CH ₃ CN	15 mg/0.1 mmol	300 W Xe lamp (no filter), 10 h	42.0	>99	42	140 ^a
2	n-NH ₂ -MIL-125 (ref. 42)	CH ₃ CN	10 mg/0.2 mmol	300 W Xe lamp (no filter), 9 h	98.5	99	97.5	1063
3	m-NH ₂ -MIL-125 (ref. 42)	CH ₃ CN	10 mg/0.2 mmol	300 W Xe lamp (no filter), 12 h	62.8	92.6	58.15	475
4	Ti-PMOF-DMA ⁴³	CH ₃ CN	5 mg/0.3 mmol	623 \pm 8 nm, 0.5 h	94.0	88	82.7	49 620 ^a
5	Ru(bpy) ₃ @MIL-125 (ref. 44)	CH ₃ CN	5 mg/0.1 mmol	Visible light (>440 nm), 3 h	75	>99	74.2	2473 ^a
6	UiO-66-NH ₂ (ref. 45)	CH ₃ CN	15 mg/0.1 mmol	300 W Xe lamp (no filter), 10 h	83.0	>99	82.2	274
7	LTG-NiRu ⁴⁶	DMF	1 mmol%/0.5 mmol	300 W Xe lamp (420–780 nm), 1 h	>99	>99	99%	—
8	Zr-NDI-PCOOH ⁴⁷	CH ₃ CN	10 mg/0.4 mmol	300 W Xe lamp (full wavelength), 0.75 h	90	100	90	24 000 ^a
9	UiO-68-BT ⁴⁸	CH ₃ CN	5 mg/0.3 mmol	415 nm (3 W \times 4), 0.42 h	96	99	95	67 857 ^a
10	This work (UiO-67 Ru ₅₀ -Mn ₁₀)	CH ₃ CN/ H ₂ O	1 mg/0.7 mmol	460 nm (LED 800–1250 mW), 24 h	53	85	45.1	6895
		CH ₃ CN			15.5	94	14.6	2229

^a The oxidative coupling rate ($\mu\text{mol g}_{\text{MOF}}^{-1} \text{h}^{-1}$) for MOFs is calculated based on their respective catalyst/benzylamine ratio, reaction time and *N*-benzylidene-1-phenylmethanamine yield reported in the literature.

many of the reference MOFs, such as Ti-PMOF-DMA, Zr-NDI-PCOOH, and UiO-68-BT (Table 3 entries 4, 8, and 9), employ novel linker systems and often involve higher synthetic complexity, which may also contribute to their enhanced activity. It is important to note, however, that other experimental factors, particularly the light source characteristics (power and wavelength), were not normalised across these studies, and such variations may exert a significant influence on catalytic performance. Taking this into account, the activity of UiO-67 Ru₅₀-Mn₁₀ can be considered moderate when compared to those MOFs.

Recyclability test

The stability of UiO-67 Ru₅₀-Mn₁₀ during the oxidative coupling of benzylamine was found to be limited to approximately 24 h in a CH₃CN/H₂O mixture (Fig. S22). After this period, the solid MOF was almost completely dissolved, as indicated by the appearance of a transparent yellow solution (Fig. S22), which can be attributed to the leaching of photocatalytic components into the solvent. Consequently, the photocatalytic performance of the residual MOF solid recovered after the first cycle was severely diminished. When tested with fresh benzylamine in CH₃CN/H₂O (4 : 1), the recovered catalyst yielded only negligible amounts of *N*-benzylidene-1-phenylmethanamine in the second cycle. Such structural collapse of MOFs in aqueous environments is a commonly encountered issue, which may occur either through chemical decomposition or under light irradiation. The dissolution can arise from competitive coordination of $\cdot\text{OH}$ radicals or amine substrates with the Zr-SBUs, leading to framework breakdown.^{38,49}

In contrast, UiO-67 Ru₅₀-Mn₁₀ exhibited recyclability in pure CH₃CN (Fig. S23). In this case, the solid MOF could be separated from the reaction medium by centrifugation, washed with CH₃CN (twice), and reused for further photocatalytic cycles with fresh benzylamine. Although the oxidative coupling of

benzylamine in pure CH₃CN proceeded with lower efficiency (14.6% yield, 2229 $\mu\text{mol g}_{\text{MOF}}^{-1} \text{h}^{-1}$), corresponding to nearly three times lower activity compared to the CH₃CN/H₂O system, the catalyst maintained stable performance over multiple cycles without significant loss of photocatalytic activity (Fig. 7).

Charge and energy transfer dynamics

Oxygen (O₂) is known as an acceptor to quench the photoexcited photosensitizer *via* energy and/or electron transfer, generating the reactive oxygen species $^1\text{O}_2$ or $\text{O}_2^{\cdot-}$ respectively.^{39,50,51} To validate these, the [Ru] complex was investigated in homogeneous CD₃CN/CD₃OD (4 : 1 v/v) solution by photoluminescence

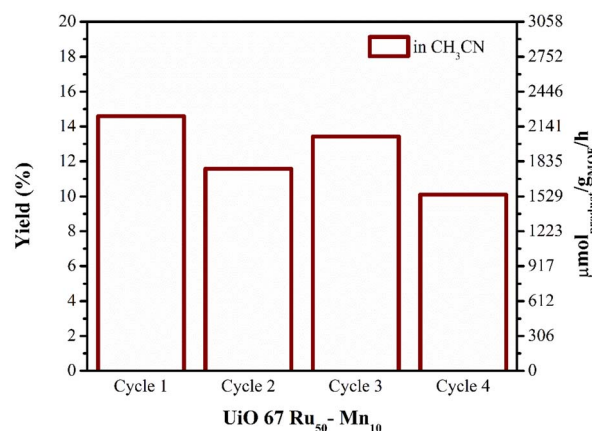


Fig. 7 Recyclability test of the UiO-67 Ru₅₀-Mn₁₀ MOF for the photocatalytic benzylamine oxidative coupling reaction: yield% and $\mu\text{mol g}_{\text{MOF}}^{-1} \text{h}^{-1}$ vs. time in CH₃CN (reaction conditions: 1 mg of MOF, λ : 460 nm LED source). After each cycle (24 hours of irradiation), the solid was separated from the solution by centrifugation at 7000 rpm, washed with CH₃CN (twice), and re-irradiated with fresh 0.734 mmol of benzylamine in 4 mL of CH₃CN.



(PL) spectroscopy in the presence and absence of [Mn] counterparts under both air and Ar atmospheres. The $^3\text{MLCT}$ emission of the photosensitizer at 640 nm and the characteristic $^1\text{O}_2$ emission at 1277 nm were monitored (Fig. 8a and b). The assignment of the $^1\text{O}_2$ emission was confirmed by comparison with the PL spectra of a standard $[\text{Ru}(\text{bpy})_3]^{2+}$ solution in CD_3CN (Fig. 8b). Consistent with the behaviour of $[\text{Ru}(\text{bpy})_3]^{2+}$ (Fig. S24), the $^3\text{MLCT}$ emission at 640 nm was significantly quenched under air relative to Ar, by $\sim 50\%$ for [Ru] alone and $\sim 30\%$ for the [Ru] + [Mn] system (Fig. 8a). Interestingly, $^1\text{O}_2$ emission at 1277 nm was detected for [Ru] alone, suggesting energy transfer (EnT) from the $^3\text{MLCT}$ state to ground-state $^3\text{O}_2$. Nevertheless, an electron transfer (ET) pathway from the $^1\text{MLCT}$ state cannot be excluded, since in the [Ru] + [Mn] system the $^3\text{MLCT}$ emission was quenched (by $\sim 30\%$) without a corresponding increase in $^1\text{O}_2$ generation (Fig. 8b). Additionally, [Mn] itself was found to quench PL of [Ru] by $\sim 50\%$ even under Ar atmosphere, highlighting its critical role in facilitating ET processes within the [Ru] + [Mn] system under both aerobic and anaerobic conditions.

Therefore, only photoluminescence (PL) spectra and time-resolved PL measurements were conducted on the MOFs to evaluate the charge separation efficiency of photo-excited electron-hole pairs (see SI for experimental details), and all measurements concerning the charge transfer between photo-excited Ru-photosensitizer and Mn were performed under an inert Ar atmosphere. As depicted in Fig. 8c, the MOF sample UiO-67- Ru_{50} , containing only the $[\text{Ru}(\text{bpy})_2(\text{bpydc})]\text{Cl}_2$ photosensitizer, exhibited strong phosphorescence emissions centred at 639 nm in CH_3CN and 648 nm in H_2O upon photoexcitation at 450 nm. In contrast, the phosphorescence intensity of UiO-67- Ru_{50} - Mn_{10} , which incorporates both the PS and $[\text{Mn}(\text{bpy})(\text{bpydc})]\text{Cl}_2$ redox-active unit, was significantly reduced in both of these solvents, and consistent with the observations made for the homogeneous [Ru] + [Mn] models.

Time-resolved PL measurements are shown in Fig. 8d and summarized in Table 4, with detailed fitting parameters provided in Table S7. In CH_3CN , the $^3\text{MLCT}$ lifetime of the Ru-based photosensitizer decreased from 246 ns in UiO-67 Ru_{50} to 62 ns in UiO-67 Ru_{50} - Mn_{10} . Similarly, in H_2O , the lifetime was

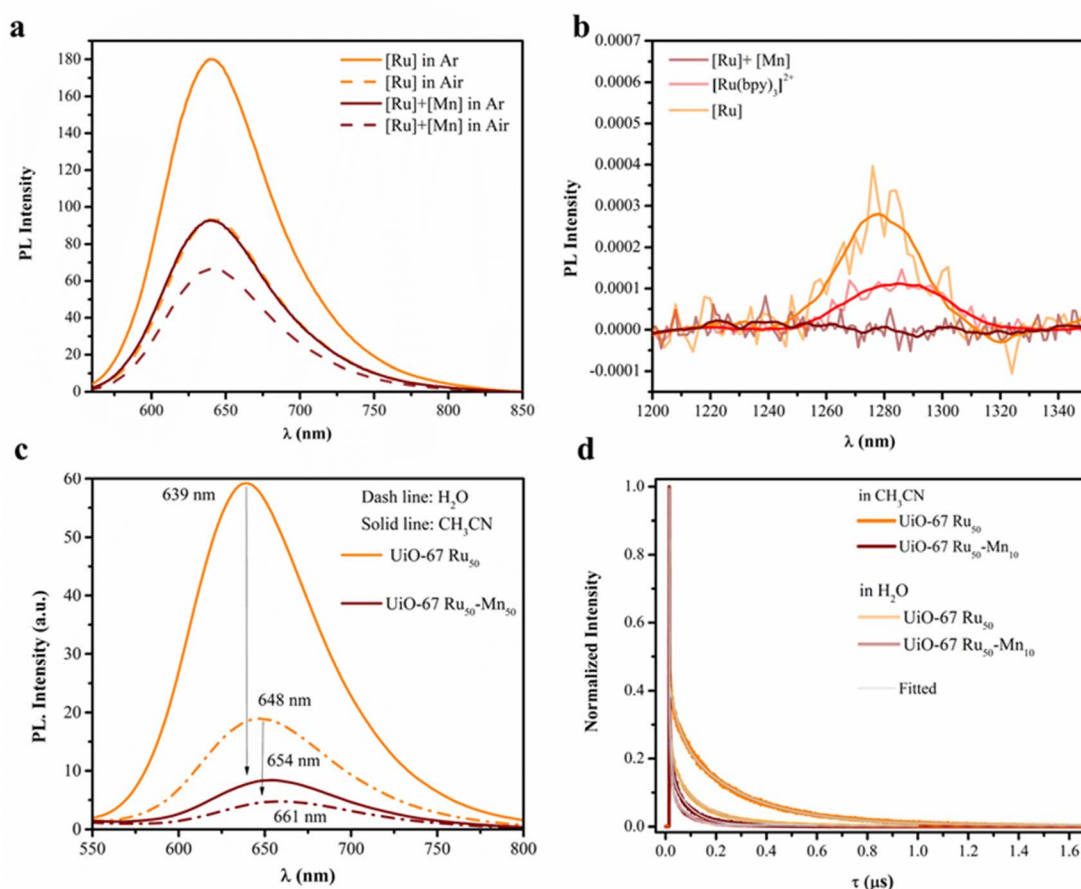


Fig. 8 (a) PL spectra of 500 μM [Ru] complex ($[\text{Ru}(\text{bpy})_2(\text{bpydc})]\text{Cl}_2$) recorded in the 550–800 nm region in the presence and absence of 500 μM [Mn] counterpart ($[\text{Mn}(\text{bpy})_2\text{Cl}_2]\text{H}_2\text{O}$) under both air and Ar atmospheres in $\text{CD}_3\text{CN}/\text{CD}_3\text{OD}$ (4 : 1 v/v) acquired at $\lambda_{\text{ex}} = 450$ nm. (b) PL spectra of 500 μM [Ru] alone and with 500 μM [Mn], monitored in the 1200–1350 nm region under air in $\text{CD}_3\text{CN}/\text{CD}_3\text{OD}$, acquired at $\lambda_{\text{ex}} = 450$ nm. For reference, a standard 500 μM $[\text{Ru}(\text{bpy})_3]^{2+}$ solution in CD_3CN is included (red solid line). All spectra in (b) were smoothed. (c) PL ($\lambda_{\text{ex}} = 450$ nm) and (d) time-resolved PL ($\lambda_{\text{ex}} = 372$ nm with a 495 nm long pass filter) spectra of UiO-67 Ru_{50} and UiO-67 Ru_{50} - Mn_{10} in deaerated CH_3CN and H_2O ([MOF] = 0.125 mg mL^{-1}).



Table 4 Table of photophysical characterization of the [Ru(bpy)₂(bpydc)]Cl₂ in homogeneous conditions and UiO-67 Ru₅₀ and UiO-67 Ru₅₀-Mn₁₀ MOF. All measurements were carried out in deaerated solvents. For a homogeneous solution, 50 μM of [Ru(bpy)₂(bpydc)]Cl₂ was used

Compounds		¹ MLCT absorption	Optical gap	³ MLCT emission	
		λ _{max} (nm)	E _g = E _{HOMO-LUMO} (eV)	λ (nm)	τ _{av} (ns)
[Ru(bpy) ₂ (bpydc)]Cl ₂	CH ₃ CN	460	2.45	615	750
	H ₂ O	450	—	670	23
UiO-67 Ru ₅₀	CH ₃ CN	446 ^a	2.10 ^b	639	246
	H ₂ O			648	112
UiO-67 Ru ₅₀ -Mn ₁₀	CH ₃ CN	444 ^a	2.10 ^b	654	62
	H ₂ O			661	47

^a Absorption spectra acquired from the diffuse reflectance spectroscopy of the MOF in the solid state. ^b Optical energy gaps (E_g) of the solids were estimated from the Kubelka Munk functions.

reduced from 112 ns to 47 ns, as summarized in Table 4. Both of these results demonstrate that the quenching of PS emission in UiO-67 Ru₅₀-Mn₁₀ arises from accelerated decay of the ³MLCT excited state, driven by efficient, solvent-independent interaction and likely reductive electron transfer between the [Ru^{II}]* and [Mn^{II}] complexes within the MOF framework. However, various studies suggest that, in the presence of external electron acceptors like methyl viologen or O₂, an oxidative quenching pathway from [Ru^{II}]* to [Ru^{III}] is followed by electron transfer (ET) from the donor Mn²⁺ in homogeneous systems.^{22,52–54}

To evaluate the influence of solvent environment and framework effects, steady-state and time-resolved PL spectroscopy of the [Ru] complex were performed in CH₃CN and H₂O under Ar atmosphere and compared with the corresponding measurements for the MOFs. The homogeneous [Ru] complex in CH₃CN exhibits phosphorescence peaks centred at 615 nm and 670 nm in CH₃CN and H₂O, respectively, with corresponding excited-state (³MLCT) lifetimes of 750 ns and 23 ns (Fig. S27 and Table 4). Interestingly, both MOF systems in CH₃CN exhibited significantly shorter ³MLCT lifetimes relative to the homogeneous Ru-complex, implying the impact of the MOF platform. However, the homogeneous complex showed a much faster decay in H₂O, indicating its lower stability of the ³MLCT state in aqueous media compared to the MOF systems. These findings highlight two key points: (i) solvent molecules significantly influence the ³MLCT state lifetimes, and (ii) the MOF framework provides enhanced stability and lifetime control for the photosensitizer in aqueous environments.

Furthermore, cyclic voltammetry (CV) experiments were conducted on the individual complexes in CH₃CN under both Ar and air atmospheres to gain further insight into the electron transfer processes. In the CV profile of [Ru(bpy)₂(bpydc)]Cl₂ (Fig. 9a and S28a), three distinct reduction peaks were observed at −1.60 V, −1.90 V, and −2.13 V vs. Fc/Fc⁺, corresponding to the successive reductions of the ligand in Ru-based photosensitizer (PS), as summarized vs. NHE in Table S8.^{52,55} An oxidation peak attributed to the Ru²⁺/Ru³⁺ redox couple (HOMO level) was also detected at +0.84 V vs. Fc/Fc⁺ (Fig. 9b).⁵⁵ The estimated HOMO and LUMO energy levels are to be +1.53 V, and −0.91 V vs. NHE, respectively (Fig. 9c). For [Mn(bpy)₂Cl₂]·H₂O, a well-

defined oxidation peak corresponding to the Mn²⁺ to Mn³⁺ transition appeared at +0.41 V vs. Fc/Fc⁺ (+1.10 V vs. NHE) (Fig. S28b and 9b), which is consistent with previously reported values.^{52,54,55} Notably, this oxidation potential +1.10 V vs. NHE is slightly less positive than the estimated HOMO level (+1.53 V vs. NHE) of [Ru(bpy)₂(bpydc)]Cl₂, indicating a thermodynamically favourable pathway for electron transfer from Mn²⁺ to the oxidized Ru³⁺ species. Under an O₂ atmosphere, an additional reduction peak attributable to the O₂/O₂^{•−} couple at −1.17 V vs. Fc/Fc⁺ (−0.48 V vs. NHE)^{56,57} was observed in the CV of [Ru(bpy)₂(bpydc)]Cl₂ (Fig. 9a and S28c). The LUMO level of the Ru-complex (−0.91 V vs. NHE) lies higher in energy than the O₂/O₂^{•−} redox couple (−0.48 V vs. NHE), providing a driving force for electron transfer from the excited ¹MLCT Ru-PS to molecular oxygen (Fig. 9c). These observations suggest that electron transfer from Ru-PS to O₂, followed by Mn²⁺ to the oxidized Ru centre, or *vice versa*, is both energetically feasible.

As the ET processes from the excited state are expected to be kinetically fast, we conducted nanosecond transient absorption spectroscopy of the [Ru] complex in CH₃CN/H₂O in the presence and absence of [Mn], and under aerobic and anaerobic conditions. The spectra shown in Fig. 10 and S25 were recorded with a delay of 100 ns after the laser pulse (λ = 450 nm). For the [Ru] complex alone in aqueous environment under Ar, the spectrum showed a ground-state bleach (GSB) at 450 nm and excited-state absorption at around 400 nm, along with two new positive absorption features centred at around 550 nm and around 800 nm, corresponding to reduced [Ru]^{•+} and solvated electron (e_{solv}), respectively.^{58–60} Notably, these species are the common photolyzed intermediates that originate in an aqueous environment and lead to decomposition.⁵⁸ Interestingly, when the spectra were acquired in the presence of [Mn] under Ar, the absorption band centred at 550 nm increased, accompanied by a decrease in GS bleach. This clearly indicates an increase in the formation of a reduced PS ([Ru]^{•+}), confirming electron transfer to the PS, *i.e.*, the excited state of [Ru] is reductively quenched. It is further notable that when both systems ([Ru] alone and [Ru] + [Mn]) were purged with air, a decrease in the absorption band in this region was observed. This effect was more pronounced in the [Ru] + [Mn] system, irrespective of the sequence of addition



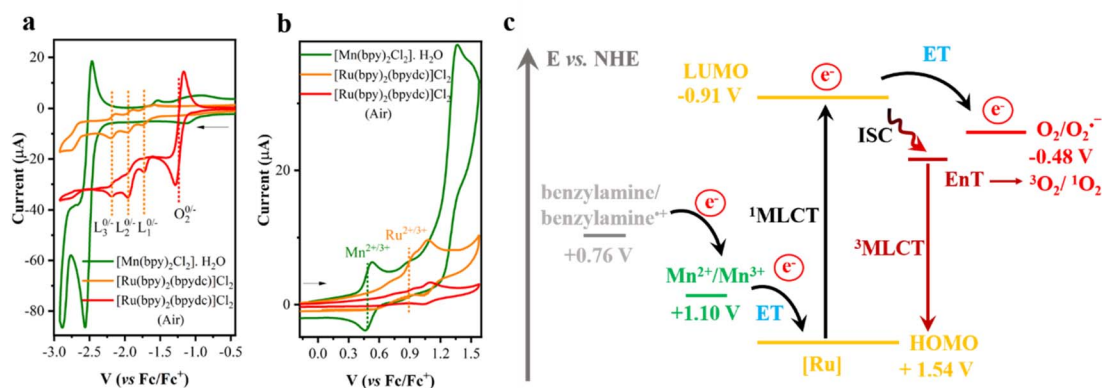


Fig. 9 (a and b) Cyclic voltammograms of [Ru(bpy)₂(bpydc)]Cl₂ (orange), [Ru(bpy)₂(bpydc)]Cl₂ in air (red), and [Mn(bpy)₂Cl₂]·H₂O (green) recorded at a scan rate of 50 mV s⁻¹. Experimental conditions: CH₃CN, 0.1 M *n*Bu₄NPF₆ as supporting electrolyte, 0.25 mM analyte concentration, glassy carbon working electrode, Pt wire counter electrode, and Ag/AgCl quasi-reference electrode referenced against Fc/Fc⁺. (c) Schematic energy level diagram illustrating (1) electron transfer (ET) from the excited [Ru(bpy)₂(bpydc)]Cl₂ to O₂, followed by ET from [Mn(bpy)₂Cl₂]·H₂O to the oxidized Ru complex (or *vice versa*), resulting in the formation of superoxide radical (O₂^{•-}) and (2) singlet oxygen (¹O₂) via energy transfer (EnT).

of [Mn] and air. These results suggest that O₂ acts as an electron acceptor, reverting the reduced PS to its ground state. This observation not only supports the validity of the initial reductive quenching mechanism but also illustrates the second step of the electron transfer process occurring between light-driven and dark reactions. Collectively, the results indicate that the PS is quenched by [Mn] *via* a reductive quenching mechanism, with no clear evidence of oxidative quenching.

Additionally, in the stimulated ³MLCT emission (SE) region around 660 nm,⁶¹ a significant negative bleaching effect was observed under aerobic conditions, more prominently in the [Ru] + [Mn] system, supporting the partial energy transfer mechanism as well in the photocatalytic systems.

Electrochemical study and ns-transient absorption spectroscopy confirm that electron transfer thermodynamics are evident under homogeneous conditions. These homogeneous studies provide essential reference points for interpreting the corresponding behaviour of the components in the MOF framework. The integration of Ru- and Mn-complexes into a unified UiO-67 framework (UiO-67 Ru₅₀-Mn₁₀) retains this synergistic character, as shown by phosphorescence quenching experiments (Fig. 8c, d and Table 4) by comparing between UiO-67 Ru₅₀ and UiO-67 Ru₅₀-Mn₁₀. However, a comparison between homogeneous vs. MOF systems clearly highlights the contribution of the MOF (Table 4). The spatial proximity of Ru and Mn within the framework facilitates more efficient electron transfer

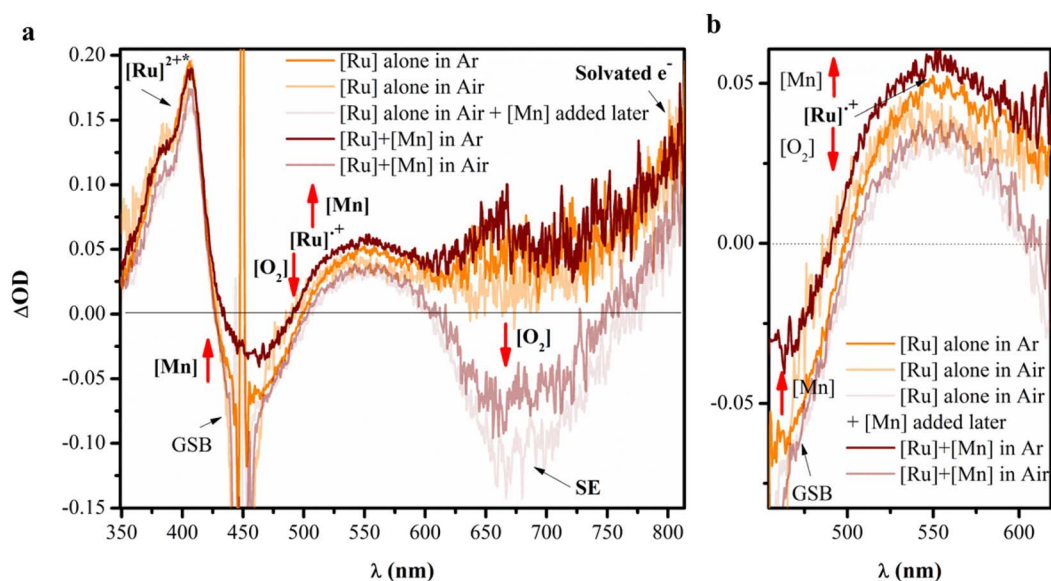


Fig. 10 (a) Transient absorption spectra of 500 μM [Ru] complex ([Ru(bpy)₂(bpydc)]Cl₂) alone and with 500 μM [Mn] ([Mn(bpy)₂Cl₂]·H₂O) in CH₃CN/H₂O (4 : 1 v/v) at a time delay of 100 ns under Ar, and air. (λ_{pump} = 450 nm). (b) Enlarged view of the spectra in the 450–610 nm region (GSB: ground state bleach, SE: stimulated emission).



than in homogeneous [Ru] + [Mn] systems, while the rigid architecture of the MOF enhances the stability of the photoactive units compared to homogeneous conditions, particularly in a CH₃CN/H₂O.

Although the ³MLCT states of Ru-complexes are not energetically suitable for O₂^{•−} formation,³⁹ they can undergo energy transfer with ambient ³O₂ to produce ¹O₂.⁶² This EnT mechanism is more prominent in CH₃CN and homogeneous systems than in MOFs.⁴⁰

Spectroscopic and photocatalytic results and intermediate identification across solvent environments suggest both electron transfer (ET) and energy transfer (EnT) pathways can operate in UiO-67 Ru₅₀-Mn₁₀ to convert benzylamine and O₂ into *N*-benzylidene-1-phenylmethanamine (Fig. 11). In the ET pathway (Fig. 11 and S14–S21): photoexcitation converts [Ru^{II}] to [Ru^{II}]* (¹MLCT), which is reduced by [Mn^{II}] to generate [Ru]^{•+} and becomes [Mn^{III}]. O₂ accepts an electron to [Ru]^{•+} to regenerate [Ru^{II}], by becoming O₂^{•−}. [Mn^{III}] (*E*^o = +1.10 V vs. NHE) oxidizes benzylamine (*E*^o = +0.76 V vs. NHE) to benzylamine radical (PhCH₂NH₂^{•+}), which reacts with O₂^{•−} to form phenylmethanimine (Im₁) and H₂O₂. In the EnT pathway (Fig. 11, bottom): ³O₂ formed *via* ³MLCT of [Ru^{II}]* reacts with benzylamine to yield the same intermediates. Formation of H₂O₂ through ¹O₂ and O₂^{•−} is well established and was also confirmed for the UiO-67 Ru₅₀-Mn₁₀ MOF using the TiOSO₄ method^{63,64} (see SI and Fig. S29). Finally, phenylmethanimine, formed *via* both pathways, undergoes a condensation reaction to generate the hemiaminal intermediate (Im₂), which subsequently eliminates NH₃ to yield the final product. It is hypothesised that the rapid decay of intermediates in pure CH₃CN prevents their detection in both the UiO-67 Ru₅₀-Mn₁₀ MOF and the homogeneous systems. In contrast, in CH₃CN/H₂O the

decay of intermediates is relatively slower, enabling their observation (Fig. 6 and S14–S21).

UiO-67 Ru₅₀-Mn₁₀ exhibits significantly enhanced photocatalytic performance, showing ~3.1, 1.65, and ~1.8-fold higher TON than [Ru] alone, [Ru] + [Mn], and UiO-67 Ru₅₀, respectively, in CH₃CN/H₂O. The superior photocatalytic activity of UiO-67 Ru₅₀-Mn₁₀ over UiO-67 Ru₅₀, homogenous [Ru] alone, and [Ru] + [Mn] systems in CH₃CN/H₂O reflects a prominent role of the ET pathways and the role of Mn in facilitating ET for the primary one-electron oxidation of benzylamine. This role of manganese as an electron transfer mediator was previously reported.⁶⁵

While the homogeneous system in CH₃CN shows superior activity than MOFs due to a more efficient EnT *via* ³MLCT, Mn remains critical in both solvent systems for promoting oxidation, thereby enhancing overall reaction kinetics in both [Ru] + [Mn] and UiO-67 Ru₅₀-Mn₁₀ compared to systems without Mn.

Conclusion

This study demonstrates that incorporating Mn²⁺ into a Ru(bpy)₃²⁺-functionalized MOF (UiO-67 Ru₅₀-Mn₁₀) significantly enhances the photocatalytic oxidation of benzylamine to *N*-benzylidene-1-phenylmethanamine by O₂ from the air in CH₃CN/H₂O, achieving a TON of 634, approximately 1.65 times higher than the homogeneous system and 1.8 times higher than the Ru-only MOF (UiO-67 Ru₅₀). Mechanistic investigations reveal the coexistence of electron transfer (ET) and energy transfer (EnT) pathways, with their relative contributions strongly influenced by the solvent environment. The CH₃CN/H₂O (4 : 1) solvent system plays a critical role by improving the polarity of the reaction medium, which collectively facilitates faster and more efficient charge separation and electron

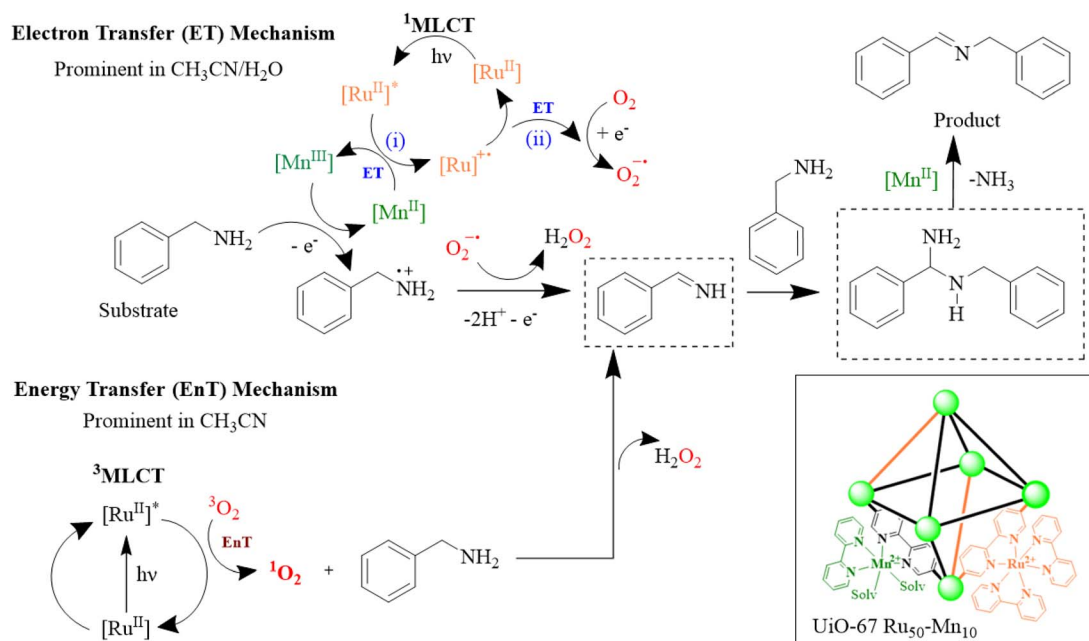


Fig. 11 Oxidative amine coupling reaction mechanisms through the electron transfer (ET) and energy transfer (EnT) pathways.

transfer. While homogeneous systems benefit more in pure CH₃CN due to faster energy transfer (EnT), the MOF-based catalyst performs best in the mixed solvent due to stabilized intermediates and enhanced electron transfer pathways (ET). Spectroscopic and electrochemical studies further confirm enhanced photostability and charge dynamics in the MOF system. The MOF system provides all advantages of MOFs, being a dispersible, highly porous materials that maintains the molecular functions of its building blocks and has the potential for easy recyclability. The cooperative interaction between Ru and Mn centres within the robust MOF framework provides a blueprint for designing efficient, photocatalysts using earth-abundant catalysts for sustainable oxidative chemistry.

Experimental section

Synthesis of UiO-67

The zirconium-based metal-organic framework (UiO-67) was synthesized *via* a solvothermal method with slight modifications from previously reported procedures.⁶⁶ ZrCl₄ (260 mg, 1.12 mmol) and benzoic acid (6.8 g, 56 mmol, 50 equiv.) were added to 50 mL of *N,N*-dimethylformamide (DMF) in a 100 mL round-bottom flask and sonicated for 10 minutes to ensure uniform dispersion and partial dissolution of the precursors. In a separate vessel, 2,2'-bipyridine-5,5'-dicarboxylic acid (H₂bpydc, 282 mg, 1.16 mmol) was suspended in 20 mL of DMF. Due to limited solubility, triethylamine (up to 320 μ L) was added incrementally (20 μ L per addition) under stirring until a clear solution was achieved. The linker solution was then slowly added to the ZrCl₄-benzoic acid mixture with continuous stirring. After 10 minutes of additional mixing, the complete reaction solution was transferred to a 100 mL Teflon-lined stainless-steel autoclave and heated at 120 $^{\circ}$ C for 72 hours under static conditions. After cooling to room temperature, the resulting crystalline solid was collected by centrifugation at 4440 rpm and washed with fresh DMF (40 mL), followed by a second centrifugation. The solid was soaked in ethanol (40 mL) overnight to promote solvent exchange, and then washed three additional times each with ethanol and acetone to remove residual modulators and solvents. Each washing step was followed by centrifugation at 4400 rpm. The purified product was dried under vacuum and further dried at 60 $^{\circ}$ C in an oven before characterization or further use. The final yield was 298.4 mg, corresponding to a 75% yield based on ZrCl₄ (theoretical yield: 398.1 mg).

Synthesis of Ru(bpy)₃²⁺-functionalized MOF (UiO-67 Ru₁₀ and UiO-67 Ru₅₀)

With a slight modification reported from the literature⁶⁶ 65 mg of ZrCl₄ (0.28 mmol) and 1.7 g of benzoic acid (14 mmol, 50 mol equiv.) were dissolved by sonication (5 min) in 10 mL of DMF. This was then added to a vial containing (1) 63.74 mg of H₂bpydc (0.261 mmol) and 21.12 mg of [Ru(bpy)₂(bpydc)]Cl₂ (0.029 mmol) for UiO-67 Ru₁₀ or (2) 35.41 mg of H₂bpydc (0.145 mmol) and 105.64 mg of [Ru(bpy)₂(bpydc)]Cl₂ (0.145 mmol) for UiO-67 Ru₅₀. As mentioned earlier, triethylamine (\sim 80 μ L) was

added incrementally (20 μ L per addition) under stirring until a clear solution was achieved before the mixing with the ZrCl₄-benzoic acid mixture. The solution was sonicated for an additional 5 min and transferred to a 100 mL Teflon-lined stainless-steel autoclave and heated at 120 $^{\circ}$ C for 72 hours and followed by a similar procedure used for pristine UiO-67.

Post-synthetic modification

Synthesis of Mn²⁺-doped UiO-67 Ru_x (UiO-67 Ru₁₀-Mn₁₀/UiO-67 Ru₅₀-Mn₁₀). UiO-67 Ru₁₀ or UiO-67 Ru₅₀ (60 mg) was suspended in 10 mL of ethanol in a round-bottom flask, followed by the addition of 0.015 or 0.05 mmol of 1 : 1 equiv. of MnCl₂·4H₂O and 2,2'-bipyridine (bpy). The resulting suspension was stirred under an argon atmosphere at reflux temperature for 4 h to facilitate coordination of Mn(II) to the Ru-functionalized MOF framework. Upon completion, the solid product was isolated by centrifugation, thoroughly washed with ethanol to remove any unbound metal species or ligands, and dried under vacuum before use.

Synthesis of Mn²⁺-doped UiO-67 (UiO-67 Mn₁₀). UiO-67 Mn₁₀ was synthesized by following the same procedure described for UiO-67-Ru metalation, using pristine UiO-67 (60 mg) in place of UiO-67 Ru₁₀ under identical conditions.

Photocatalytic oxidation of benzylamine. In a typical procedure, 1 mg of MOF powder was dispersed in 4 mL of a CH₃CN : H₂O (4 : 1 v/v) solvent mixture in an 8 mL vial and ultrasonicated for 5 minutes to ensure homogeneous dispersion. Subsequently, 0.734 mmol of benzylamine (80 μ L) was added using a micropipette. The reaction mixture was kept in the dark overnight at ambient conditions. After the dark period, the vial was irradiated using a 460 nm LED light source (Azula Photo-reactor, λ = 460 nm, 800–1250 mW) operating at 0.7 A and 4 V under continuous stirring.

For control experiments, the same procedure was followed by replacing the MOF catalyst with either (1) a combination of 0.28 μ mol of [Ru(bpydc)(bpy)₂]Cl₂ and 0.14 μ mol of [Mn(bpy)₂-Cl₂]H₂O, or (2) 0.28 μ mol of [Ru(bpydc)(bpy)₂]Cl₂ (0.204 mg) alone in 4 mL of CH₃CN with 0.734 mmol of benzylamine (80 μ L).

At selected time intervals (initial, 0 h (dark), 1–24 h for kinetics; and 24 h for final yield), 240 μ L aliquots were withdrawn and centrifuged at 15 000 rpm for 5 minutes to remove the solid MOF. Then, 200 μ L of the supernatant was transferred to a rotavapor vial, and CH₃CN was evaporated under reduced pressure at 50 $^{\circ}$ C, 150 rpm, gradually lowering the pressure from 230 mbar to 72 mbar, followed by full vacuum. The residue was redissolved in 800 μ L of CD₃CN containing a known quantity of internal standard (1,3,5-trioxane, 3 mg, 0.037 mmol), transferred to an NMR tube, and analysed by ¹H NMR (64 scans).

For homogeneous control reactions, the centrifugation step was omitted. After evaporation of the solvent from 200 μ L of the reaction mixture, the residue was treated with 800 μ L of CD₃CN containing the internal standard and analysed directly by ¹H NMR.

Cyclic voltammetry. Cyclic voltammetry (CV) experiments were performed on a Pine Research Wavedriver 200 electrochemical workstation equipped with a standard three-electrode



arrangement: working electrode (WE): glassy carbon electrode ($d = 3.0$ mm), quasi-reference electrode (RE): Ag/AgCl, counter electrode (CE): Pt wire. All potentials are quoted relative to the ferrocene/ferrocenium internal standard. All experiments were performed in dry acetonitrile (CH_3CN) using $n\text{Bu}_4\text{NPF}_6$ (0.1 M) as supporting electrolyte. The solutions were purged with argon for at least 15 minutes to remove O_2 and kept under a slight positive argon pressure when performing the experiments.

Conflicts of interest

There are no conflicts to declare.

Data availability

The data supporting the findings of the article including detailed experimental descriptions can be found in the supplementary information (SI). Supplementary information is available. See DOI: <https://doi.org/10.1039/d5ra04503g>.

Acknowledgements

A. P. gratefully acknowledges the Vector Stiftung (project number P2019-0110) and the Carl-Zeiss Stiftung for financial support. K. L., R. M., A. P., U. K. and J. B. gratefully acknowledge funding by the German Research Foundation (DFG) project numbers 364549901 TRR234 (CataLight B03, B08 and Z02). We thank Samuel Blessing, Anorganische Chemie II, Ulm University, for help with the powder XRD measurements. The authors also thank Renate Kunz and Paul Walther from the Central Facility for Electron Microscopy, Ulm University, for help with transmission electron microscopy measurements. Joachim Bansmann is acknowledged for XPS measurements, and we thank the Core Facility EMMA at Ulm University for providing support and access to XPS instrumentation. Lastly, we thank Dariusz Mitoraj, Institute of Electrochemistry, Universität Ulm, for the solid-state UV-visible diffuse reflectance measurement.

References

- Y. Yamamoto, S. Kodama, A. Nomoto and A. Ogawa, Innovative green oxidation of amines to imines under atmospheric oxygen, *Org. Biomol. Chem.*, 2022, **20**, 9503–9521.
- J. C. Lopes, T. Moniz, M. J. Sampaio, C. G. Silva, M. Rangel and J. L. Faria, Efficient synthesis of imines using carbon nitride as photocatalyst, *Catal. Today*, 2023, **418**, 114045.
- X. Lang, W. Ma, Y. Zhao, C. Chen, H. Ji and J. Zhao, Visible-Light-Induced Selective Photocatalytic Aerobic Oxidation of Amines into Imines on TiO_2 , *Chem.–Eur. J.*, 2012, **18**, 2624–2631.
- P. M. Stanley, J. Haimel, C. Thomas, A. Urstoeger, M. Schuster, N. B. Shustova, A. Casini, B. Rieger, J. Warnan and R. A. Fischer, Host–Guest Interactions in a Metal–Organic Framework Isorecticular Series for Molecular Photocatalytic CO_2 Reduction, *Angew. Chem., Int. Ed.*, 2021, **60**, 17854–17860.
- S. Mandal, S. Yoosefi, A. K. Mengele, S. Rau and A. Pannwitz, Active molecular units in metal organic frameworks for artificial photosynthesis, *Inorg. Chem. Front.*, 2024, **11**, 7682–7755.
- A. Galushchinskiy, R. González-Gómez, K. McCarthy, P. Farràs and A. Savateev, Progress in Development of Photocatalytic Processes for Synthesis of Fuels and Organic Compounds under Outdoor Solar Light, *Energy Fuels*, 2022, **36**, 4625–4639.
- F.-J. Zhao, G. Zhang, Z. Ju, Y.-X. Tan and D. Yuan, The Combination of Charge and Energy Transfer Processes in MOFs for Efficient Photocatalytic Oxidative Coupling of Amines, *Inorg. Chem.*, 2020, **59**, 3297–3303.
- D. Sun, L. Ye and Z. Li, Visible-light-assisted aerobic photocatalytic oxidation of amines to imines over $\text{NH}_2\text{-MIL-125(Ti)}$, *Appl. Catal., B*, 2015, **164**, 428–432.
- D. Bai, J. Qiu, J. Li, S. Zhou, X. Cui, X. Tang, Y. Tang, W. Liu and B. Chen, Mesoporous Mixed-Metal–Organic Framework Incorporating a $[\text{Ru}(\text{Phen})_3]^{2+}$ Photosensitizer for Highly Efficient Aerobic Photocatalytic Oxidative Coupling of Amines, *ACS Appl. Mater. Interfaces*, 2023, **15**, 30320–30331.
- W.-J. Xu, B.-X. Huang, G. Li, F. Yang, W. Lin, J.-X. Gu, H.-G. Deng, Z.-G. Gu and H.-G. Jin, Donor–Acceptor Mixed-Naphthalene Diimide–Porphyrin MOF for Boosting Photocatalytic Oxidative Coupling of Amines, *ACS Catal.*, 2023, **13**, 5723–5732.
- Y. An, X. Lv, W. Jiang, L. Wang, Y. Shi, X. Hang and H. Pang, The stability of MOFs in aqueous solutions—research progress and prospects, *Green Chem. Eng.*, 2024, **5**, 187–204.
- C.-C. Hou, T.-T. Li, S. Cao, Y. Chen and W.-F. Fu, Incorporation of a $[\text{Ru}(\text{dcbpy})(\text{bpy})_2]^{2+}$ photosensitizer and a $\text{Pt}(\text{dcbpy})\text{Cl}_2$ catalyst into metal–organic frameworks for photocatalytic hydrogen evolution from aqueous solution, *J. Mater. Chem. A*, 2015, **3**, 10386–10394.
- S. Yang, B. Pattengale, S. Lee and J. Huang, Real-Time Visualization of Active Species in a Single-Site Metal–Organic Framework Photocatalyst, *ACS Energy Lett.*, 2018, **3**, 532–539.
- M. Liu, Y.-F. Mu, S. Yao, S. Guo, X.-W. Guo, Z.-M. Zhang and T.-B. Lu, Photosensitizing single-site metal–organic framework enabling visible-light-driven CO_2 reduction for syngas production, *Appl. Catal., B*, 2019, **245**, 496–501.
- G. Lan, Z. Li, S. S. Veroneau, Y.-Y. Zhu, Z. Xu, C. Wang and W. Lin, Photosensitizing Metal–Organic Layers for Efficient Sunlight-Driven Carbon Dioxide Reduction, *J. Am. Chem. Soc.*, 2018, **140**, 12369–12373.
- Z. Wang, P. Yeary, Y. Fan, C. Deng and W. Lin, Active Site Isolation and Enhanced Electron Transfer Facilitate Photocatalytic CO_2 Reduction by A Multifunctional Metal–Organic Framework, *ACS Catal.*, 2024, **14**, 9217–9223.
- S. Guo, L. Kong, P. Wang, S. Yao, T. Lu and Z. Zhang, Switching Excited State Distribution of Metal–Organic Framework for Dramatically Boosting Photocatalysis, *Angew. Chem., Int. Ed.*, 2022, **61**, e202206193.
- X. Feng, Y. Pi, Y. Song, Z. Xu, Z. Li and W. Lin, Integration of Earth-Abundant Photosensitizers and Catalysts in Metal–



- Organic Frameworks Enhances Photocatalytic Aerobic Oxidation, *ACS Catal.*, 2021, **11**, 1024–1032.
- 19 Y. Umena, K. Kawakami, J.-R. Shen and N. Kamiya, Crystal structure of oxygen-evolving photosystem II at a resolution of 1.9 Å, *Nature*, 2011, **473**, 55–60.
 - 20 M. D. Kärkäs, O. Verho, E. V. Johnston and B. Åkermark, Artificial Photosynthesis: Molecular Systems for Catalytic Water Oxidation, *Chem. Rev.*, 2014, **114**, 11863–12001.
 - 21 P. Huang, A. Magnuson, R. Lomoth, M. Abrahamsson, M. Tamm, L. Sun, B. van Rotterdam, J. Park, L. Hammarström, B. Åkermark and S. Styring, Photo-induced oxidation of a dinuclear Mn₂II,II complex to the Mn₂III,IV state by inter- and intramolecular electron transfer to RuIIItris-bipyridine, *J. Inorg. Biochem.*, 2002, **91**, 159–172.
 - 22 L. Hammarström, L. Sun, B. Åkermark and S. Styring, A biomimetic approach to artificial photosynthesis: Ru(II)-polypyridine photo-sensitisers linked to tyrosine and manganese electron donors, *Spectrochim. Acta, Part A*, 2001, **57**, 2145–2160.
 - 23 R. Navarro Amador, M. Carboni and D. Meyer, Sorption and photodegradation under visible light irradiation of an organic pollutant by a heterogeneous UiO-67–Ru–Ti MOF obtained by post-synthetic exchange, *RSC Adv.*, 2017, **7**, 195–200.
 - 24 X. Yu and S. M. Cohen, Photocatalytic metal–organic frameworks for the aerobic oxidation of arylboronic acids, *Chem. Commun.*, 2015, **51**, 9880–9883.
 - 25 N. Ko, J. Hong, S. Sung, K. E. Cordova, H. J. Park, J. K. Yang and J. Kim, A significant enhancement of water vapour uptake at low pressure by amine-functionalization of UiO-67, *Dalton Trans.*, 2015, **44**, 2047–2051.
 - 26 J. Zhou, S. Gu, Y. Xiang, Y. Xiong and G. Liu, UiO-67: A versatile metal-organic framework for diverse applications, *Coord. Chem. Rev.*, 2025, **526**, 216354.
 - 27 S. Mandal, A. Deshpande, R. Leiter, J. Biskupek, U. Kaiser and A. Pannwitz, Enhanced and Durable Light-Driven Hydrogen Evolution by Cobalt-Based Prussian Blue Analogs in Phospholipid Bilayers, *Adv. Energy Sustainability Res.*, 2025, **6**, 2400372.
 - 28 P. Chakraborty, I. Majumder, K. S. Banu, B. Ghosh, H. Kara, E. Zangrando and D. Das, Mn(II) complexes of different nuclearity: synthesis, characterization and catecholase-like activity, *Dalton Trans.*, 2016, **45**, 742–752.
 - 29 K. Hemmer, H. L. B. Boström, S. Krause, B. V. Lotsch and R. A. Fischer, Strategies to achieve reproducible synthesis of phase-pure Zr-porphyrin metal-organic frameworks, *Commun. Mater.*, 2024, **5**, 264.
 - 30 S. Mandal, R. Leiter, J. Biskupek, U. Kaiser and A. Pannwitz, The Zr₆O₆ Secondary Building Unit and Porphyrin Linker Catalyze Light-Driven H₂ Evolution in Porphyrin-Based Metal Organic Frameworks, *ChemSusChem*, 2025, **18**, e202500372.
 - 31 D. K. Sannes, S. Øien-Ødegaard, E. Aunan, A. Nova and U. Olsbye, Quantification of Linker Defects in UiO-Type Metal–Organic Frameworks, *Chem. Mater.*, 2023, **35**, 3793–3800.
 - 32 Q. Yang, Y. Wang, J. Wang, F. Liu, N. Hu, H. Pei, W. Yang, Z. Li, Y. Suo and J. Wang, High effective adsorption/removal of illegal food dyes from contaminated aqueous solution by Zr-MOFs (UiO-67), *Food Chem.*, 2018, **254**, 241–248.
 - 33 X. Dong, Y. Lin, Y. Ma and L. Zhao, Ce-doped UiO-67 nanocrystals with improved adsorption property for removal of organic dyes, *RSC Adv.*, 2019, **9**, 27674–27683.
 - 34 H. Zhang, W. Chen, X. Zou, Q. Sun and E. Gao, A Novel Copper-Functionalized MOF Modified Composite Electrode for High-Efficiency Detection of Nitrite and Histamine, *J. Electrochem. Soc.*, 2022, **169**, 077511.
 - 35 S. Su, Y. Cao, Y. Ren, H. Jiang and W. Wu, Tuning the electronic states of Pd(II) defect-engineered metal-organic framework catalysts for efficient conversion of isocyanides, *Commun. Chem.*, 2025, **8**, 105.
 - 36 M. Fujiwara, T. Matsushita and S. Ikeda, Evaluation of Mn3s X-ray photoelectron spectroscopy for characterization of manganese complexes, *J. Electron Spectrosc. Relat. Phenom.*, 1995, **74**, 201–206.
 - 37 Q. Sun, M. Liu, K. Li, Y. Han, Y. Zuo, F. Chai, C. Song, G. Zhang and X. Guo, Synthesis of Fe/M (M = Mn, Co, Ni) bimetallic metal organic frameworks and their catalytic activity for phenol degradation under mild conditions, *Inorg. Chem. Front.*, 2017, **4**, 144–153.
 - 38 X. Jiang, W. Wang, H. Wang, J. Zhu, Z.-H. He, Y. Yang, K. Wang and Z.-T. Liu, Solvent-free direct aerobic photocatalytic ammoxidation of benzyl alcohol to benzonitrile on In₂O₃/Au/POCN, *J. Catal.*, 2025, **442**, 115861.
 - 39 J. Zhu, W. A. Maza and A. J. Morris, Light-harvesting and energy transfer in ruthenium(II)-polypyridyl doped zirconium(IV) metal-organic frameworks: A look toward solar cell applications, *J. Photochem. Photobiol., A*, 2017, **344**, 64–77.
 - 40 I. M. M. de Carvalho and M. H. Gehlen, The solvent effect on electronic energy transfer between excited [Ru(bpy)₃]²⁺ donor and aromatic acceptors, *J. Photochem. Photobiol., A*, 1999, **122**, 109–113.
 - 41 R. Liu, S. Meng, Y. Ma, L. Niu, S. He, X. Xu, B. Su, D. Lu, Z. Yang and Z. Lei, Atmospheric oxidative coupling of amines by UiO-66-NH₂ photocatalysis under milder reaction conditions, *Catal. Commun.*, 2019, **124**, 108–112.
 - 42 X. Tan, J. Zhang, J. Shi, X. Cheng, D. Tan, B. Zhang, L. Liu, F. Zhang, B. Han and L. Zheng, Fabrication of NH₂-MIL-125 nanocrystals for high performance photocatalytic oxidation, *Sustainable Energy Fuels*, 2020, **4**, 2823–2830.
 - 43 W. Sheng, F. Huang, X. Dong and X. Lang, Solvent-controlled synthesis of Ti-based porphyrinic metal–organic frameworks for the selective photocatalytic oxidation of amines, *J. Colloid Interface Sci.*, 2022, **628**, 784–793.
 - 44 X. Yang, T. Huang, S. Gao and R. Cao, Boosting photocatalytic oxidative coupling of amines by a Ru-complex-sensitized metal-organic framework, *J. Catal.*, 2019, **378**, 248–255.
 - 45 R. Liu, S. Meng, Y. Ma, L. Niu, S. He, X. Xu, B. Su, D. Lu, Z. Yang and Z. Lei, Atmospheric oxidative coupling of



- amines by UiO-66-NH₂ photocatalysis under milder reaction conditions, *Catal. Commun.*, 2019, **124**, 108–112.
- 46 D. Bai, J. Qiu, J. Li, S. Zhou, X. Cui, X. Tang, Y. Tang, W. Liu and B. Chen, Mesoporous Mixed-Metal–Organic Framework Incorporating a [Ru(Phen)₃]²⁺ Photosensitizer for Highly Efficient Aerobic Photocatalytic Oxidative Coupling of Amines, *ACS Appl. Mater. Interfaces*, 2023, **15**, 30320–30331.
 - 47 H. Jin, W. Lin, H. Sun, P. Zhao, J. Deng and Y. Liu, Post-Modification of MOF with Electron Donor for Efficient Photocatalytic Oxidative Organic Transformations, *Chem.–Eur. J.*, 2025, **31**, e202500015.
 - 48 B. Zeng, Y. Wang, F. Huang, K. Xiong, K. Zhang and X. Lang, Blue light-driven selective aerobic oxidation of amines by benzothiadiazole metal–organic framework photocatalysis, *Catal. Sci. Technol.*, 2024, **14**, 2838–2847.
 - 49 A. Dhakshinamoorthy, A. M. Asiri and H. García, Metal–Organic Framework (MOF) Compounds: Photocatalysts for Redox Reactions and Solar Fuel Production, *Angew. Chem., Int. Ed.*, 2016, **55**, 5414–5445.
 - 50 S. M. Barrett, C. Wang and W. Lin, Oxygen sensing via phosphorescence quenching of doped metal–organic frameworks, *J. Mater. Chem.*, 2012, **22**, 10329.
 - 51 C. A. Kent, D. Liu, A. Ito, T. Zhang, M. K. Brennaman, T. J. Meyer and W. Lin, Rapid energy transfer in non-porous metal–organic frameworks with caged Ru(bpy)₃²⁺ chromophores: oxygen trapping and luminescence quenching, *J. Mater. Chem. A*, 2013, **1**, 14982.
 - 52 C. Baffert, S. Dumas, J. Chauvin, J.-C. Leprêtre, M.-N. Collomb and A. Deronzier, Photoinduced oxidation of [Mn(L)₃]²⁺ and [Mn₂O₂(L)₄]³⁺ (L = 2,2'-bipyridine and 4,4'-dimethyl-2,2'-bipyridine) with the [Ru(bpy)₃]²⁺/aryl diazonium salt system, *Phys. Chem. Chem. Phys.*, 2005, **7**, 202–210.
 - 53 L. Sun, M. K. Raymond, A. Magnuson, D. LeGourriérec, M. Tamm, M. Abrahamsson, P. Huang Kenéz, J. Mårtensson, G. Stenhagen, L. Hammarström, S. Styring and B. Åkermark, Towards an artificial model for Photosystem II: a manganese(II,II) dimer covalently linked to ruthenium(II) tris-bipyridine via a tyrosine derivative, *J. Inorg. Biochem.*, 2000, **78**, 15–22.
 - 54 K. E. Berg, A. Tran, M. K. Raymond, M. Abrahamsson, J. Wolny, S. Redon, M. Andersson, L. Sun, S. Styring, L. Hammarström, H. Toftlund and B. Åkermark, Covalently Linked Ruthenium(II)–Manganese(II) Complexes: Distance Dependence of Quenching and Electron Transfer, *Eur. J. Inorg. Chem.*, 2001, **2001**, 1019–1029.
 - 55 S. Romain, C. Baffert, S. Dumas, J. Chauvin, J.-C. Leprêtre, D. Daveloose, A. Deronzier and M.-N. Collomb, Tetranuclear polybipyridyl complexes of Ru^{II} and Mn^{II}, their electro- and photo-induced transformation into di-μ-oxo Mn^{III} Mn^{IV} hexanuclear complexes, *Dalton Trans.*, 2006, 5691–5702.
 - 56 T. Zhang, W. Wang, M. He, H. Wang, Z.-H. He, Y. Yang, K. Wang and Z.-T. Liu, Boosting the solvent-free photocatalytic oxidation of benzylamine to N-benzylenebutylamine over BiOX/TiO₂ heterojunction nanoflowers, *Sep. Purif. Technol.*, 2025, **356**, 130021.
 - 57 T. Zhang, W. Wang, X. Jiang, H. Wang, Z.-H. He, Y. Yang, K. Wang, Z.-T. Liu and B. Han, Fabricating CdS/Ag/BiVO₄ Z-heterojunction for solvent-free photocatalytic oxidation of amines, *Green Chem.*, 2024, **26**, 3338–3345.
 - 58 A. N. Tarnovsky, W. Gawelda, M. Johnson, C. Bressler and M. Chergui, Photexcitation of Aqueous Ruthenium(II)-tris-(2,2'-bipyridine) with High-Intensity Femtosecond Laser Pulses, *J. Phys. Chem. B*, 2006, **110**, 26497–26505.
 - 59 M. Goez, D. von Ramin-Marro, M. H. Othman Musa and M. Schiewek, Photoionization of [Ru(bpy)₃]²⁺: A Catalytic Cycle with Water as Sacrificial Donor, *J. Phys. Chem. A*, 2004, **108**, 1090–1100.
 - 60 M. Alvaro, E. Carbonell, B. Ferrer, F. X. Llabrés i Xamena and H. Garcia, Semiconductor Behavior of a Metal–Organic Framework (MOF), *Chem.–Eur. J.*, 2007, **13**, 5106–5112.
 - 61 S. Wang, S. Xing, Z. Shi, J. He, Q. Han and M. Li, Electrostatic polypyridine–ruthenium(II)···decatungstate dyads: structures, characterizations and photodegradation of dye, *RSC Adv.*, 2017, **7**, 18024–18031.
 - 62 R. E. P. Nau, J. Bösking and A. Pannwitz, Compartmentalization Accelerates Photosensitized NADH to NAD⁺ Conversion, *ChemPhotoChem*, 2022, **6**, e202200158.
 - 63 B. J. Deadman, K. Hellgardt and K. K. (Mimi) Hii, A colorimetric method for rapid and selective quantification of peroxodisulfate, peroxomonosulfate and hydrogen peroxide, *React. Chem. Eng.*, 2017, **2**, 462–466.
 - 64 K. Wenderich, B. A. M. Nieuweweme, G. Mul and B. T. Mei, Selective Electrochemical Oxidation of H₂O to H₂O₂ Using Boron-Doped Diamond: An Experimental and Techno-Economic Evaluation, *ACS Sustain. Chem. Eng.*, 2021, **9**, 7803–7812.
 - 65 S. S. Kim, S. S. Thakur, J. Y. Song and K. H. Lee, Oxidative coupling of benzylamines into N-benzylbenzaldimines with Mn(II)/tert-BuOOH, *Bull. Korean Chem. Soc.*, 20025, **26**(3), 499–501.
 - 66 W. A. Maza and A. J. Morris, Photophysical Characterization of a Ruthenium(II) Tris(2,2'-bipyridine)-Doped Zirconium UiO-67 Metal–Organic Framework, *J. Phys. Chem. C*, 2014, **118**, 8803–8817.

